ISSN 1560-3547, Regular and Chaotic Dynamics, 2011, Vol. 16, Nos. 1–2, pp. 155–185. © Pleiades Publishing, Ltd., 2011.

Quasi-periodic Bifurcations of Invariant Circles in Low-dimensional Dissipative Dynamical Systems

Renato Vitolo[1][*], Henk Broer[2][**], and Carles Simó[3][***]

[1] *College of Engineering, Mathematics and Physical Sciences*
University of Exeter, Harrison Building, North Park Road, Exeter, EX4 4QF, UK

[2] *Johann Bernoulli Institute for Mathematics and Computer Science*
University of Groningen, PO Box 407, 9700 AK Groningen, The Netherlands,

[3] *Departament de Matemàtica Aplicada i Anàlisi*
Universitat de Barcelona
Gran Via 585, 08007 Barcelona, Spain

Received November 24, 2010; accepted December 15, 2010

Abstract—This paper first summarizes the theory of quasi-periodic bifurcations for dissipative dynamical systems. Then it presents algorithms for the computation and continuation of invariant circles and of their bifurcations. Finally several applications are given for quasi-periodic bifurcations of Hopf, saddle-node and period-doubling type.

MSC2010 numbers: `37M20, 37C55, 37G30`

DOI: `10.1134/S1560354711010060`

Key words: bifurcations, invariant tori, resonances, KAM theory

Contents

---

[*] E-mail: `r.vitolo@exeter.ac.uk`

[**] E-mail: `H.W.Broer@rug.nl`

[***] E-mail: `carles@maia.ub.es`

---

1. INTRODUCTION

The theory of computation and continuation of bifurcations in dynamical systems with discrete or continuous time is well-understood in the case of fixed points of autonomous systems and cases reducible to them, at least for small codimension. This includes cases with periodic forcing or bifurcations of periodic orbits. This is no longer true for quasi-periodic forcing or bifurcations of invariant tori. Several problems emerge here. The dense occurrence of resonances obstructs straightforward continuation methods. More alarmingly, the quasi-periodic bifurcation theory for systems that are not reducible to Floquet form has not even been understood theoretically. This paper summarizes theoretical results in the reducible case, provides algorithms for the computation and continuation of invariant circles and their bifurcations and illustrates them with several examples.

First a summary of theoretical results is given in Section 2. The simplest way to describe the differences and additional difficulties with respect to the "classical" bifurcation theory is to say that the quasi-periodicity gives rise to a "Cantorization" of the bifurcation sets in the product of state space and parameter space, owing to the dense occurrence of resonances.

The discussion of algorithms is restricted to invariant circles of maps and is given in Section 3. The basic idea is to work in a suitable Fourier space, expressing invariant circles as truncated Fourier series. We consider both the continuation of invariant circles and of their bifurcation sets which, in general, are Cantor-like. A quite delicate problem occurs when the rotation number changes during the numerical continuation: the continuation process has to "skip" the resonances, fumbling in search of suitable Diophantine rotation numbers. For the computation of bifurcations, one has to examine the normal linear behavior around the invariant circle. Hence one has to look for the reduction to Floquet form of the linear dynamics at the invariant circle.

In Section 4 these continuation methods are applied to the analyzis of a model map for the Hopf-saddle-node bifurcation of fixed points. We analyze, successively, quasi-periodic bifurcations of Hopf, saddle-node and period doubling type. A "simpler" additional case, a quasi-periodically driven Hénon map, is studied in Section 5. In that case the rotation number is fixed, thereby removing the problem of internal resonances. The challenges arise due to lack of reducibility of the normal linear dynamics. A summary of open problem is given in Section 6.

2. QUASI-PERIODIC BIFURCATION THEORY

Quasi-periodic bifurcation theory is inspired by the "classical" bifurcation theory at equilibria, fixed points and periodic orbits, for the case of invariant tori in a nearly integrable setting. The bifurcation scenarios then mimic the classical scenarios on a nowhere dense set. This set sits in the complement of infinitely many resonances occurring densely, and is defined by Diophantine conditions. In appropriate dimensions the set has positive Hausdorff dimension.

Colloquially we say that the quasi-periodic bifurcation scenario *Cantorizes* the corresponding classical scenario. In the resonant gaps typically periodicity and chaos can occur, or other forms of quasi-periodicity. In many cases similar quasi-periodic bifurcations repeat themselves at smaller and smaller scale, ad infinitum. Such scenarios abundantly occur in many examples and applications, where often the nearly integrable setting is provoked by normal form theory at equilibria or periodic orbits.

2.1. Setting of the Problem

Starting point is the bifurcation theory of equilibria and periodic orbits for either flows or maps. Moreover, preservation of structure such as a symplectic or volume form, a symmetry group (including reversible cases) are optional. Classical examples of such bifurcations are the saddle-node, the period doubling and Hopf bifurcation, as well as their structure preserving versions. Below we review the theory for the case of flows with invariant tori, but completely analogous results exist for the case of maps. In the simplest cases we then are dealing with invariant circles.

To fix thoughts we consider a parametrized C^∞–system of the form

$$\begin{aligned} \dot{x} &= \omega(\lambda) + f(x, z, \lambda) \\ \dot{z} &= \Omega(\lambda) z + h(x, z, \lambda), \end{aligned} \tag{2.1}$$

for $x \in \mathbb{T}^n = \mathbb{R}/(2\pi\mathbb{Z})^n$, $z \in \mathbb{R}^m$ and $\lambda \in \mathbb{R}^s$; the latter two variables often only are "locally" defined, in fact, z varies over a neighborhood of $z = 0$. Moreover, $|f| = O(|z|)$ and $|h| = O(|z|^2)$ as $|z| \to 0$. Integrability of such a system amounts to equivariance with respect to the $\mathbb{T}^n$ action

$$(\theta, (x, z)) \mapsto (x + \theta, z),$$

in turn meaning that f and h do not depend on x. In general the bifurcation concerns the invariant torus $z = 0$ for some specific parameter value $\lambda = \lambda_0$, i.e., the torus $\mathbb{T}^n \times \{0\} \times \{\lambda_0\} \subset \mathbb{T}^n \times \mathbb{R}^n \times \mathbb{R}^s$. For simplicity we set $\lambda_0 = 0$.

Remark. We notice that system (2.1) has a Floquet form with an x–independent normal linear part $\omega\partial_x + \Omega z \partial_z$. That such a form can be obtained, i.e., reducibility to Floquet form, is a serious restriction and it is of great interest to extend the theory to nonreducible cases. First results in this direction can be found in [14, 25, 27, 40, 41, 65], see below for some details.

By normalization or averaging techniques [4, 6] we can find integrable approximations of (2.1) of the form

$$\begin{aligned} \dot{x} &= \omega(\lambda) + \hat{f}(z, \lambda) \\ \dot{z} &= \Omega(\lambda) z + \hat{h}(z, \lambda). \end{aligned} \tag{2.2}$$

Observe that the two equations of the integrable system (2.2) decouple and the bifurcations that are particularly of the present interest are led by those of the $\mathbb{T}^n$–reduction

$$\dot{z} = \Omega(\lambda) z + \hat{h}(z, \lambda), \tag{2.3}$$

at $(z, \lambda) = (0, 0)$.

In the general "dissipative" setting these concern with loss of hyperbolicity of $\Omega(0)$. First considering the cases of lowest codimension and reduction to a center manifold this reduces to the saddle-node and the Hopf bifurcations.

Remarks.

1. In the Hamiltonian setting on $\mathbb{T}^n \times \mathbb{R}^n \times \mathbb{R}^{2p} \times \mathbb{R}^s = \{x, y, z, \lambda\}$ the counterpart of (2.1) reads

$$\begin{aligned} \dot{x} &= \omega(y, \lambda) + f(x, y, z, \lambda) \\ \dot{y} &= g(x, y, z, \lambda) \\ \dot{z} &= \Omega(y, \lambda) z + h(x, y, z, \lambda), \end{aligned}$$

   where we use the symplectic form $\sum_{j=1}^{n} dx_j \wedge dy_j + \sum_{j=1}^{p} dz_j \wedge dz_{p+j}$. In this setting the "action" variable y acts as a distinguished parameter. In many applications the sport is to see how far one can get when $s = 0$, only making use of the distinguished parameter y.

2. A unified approach to structure preserving cases is obtained by working with Lie algebras of systems [4, 14, 16, 17]: next to the general "dissipative" and the symplectic setting, also volume preserving, equivariant, reversible cases are included as well as combinations of these.

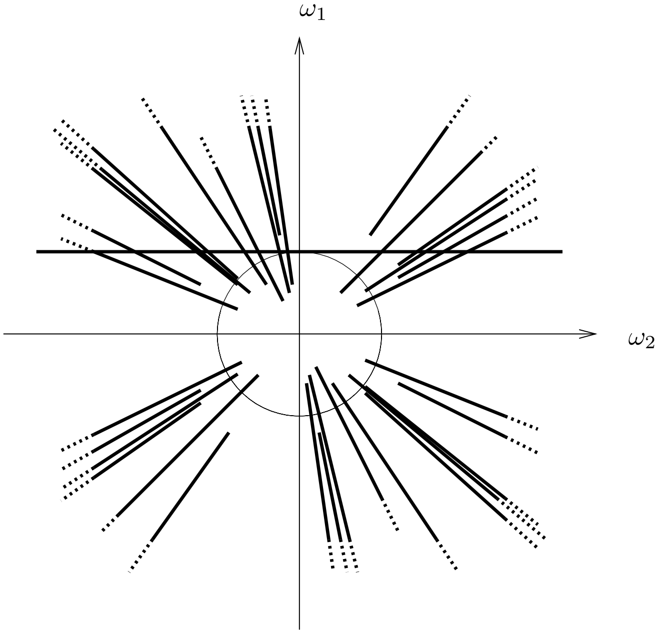

Fig. 1. Sketch of the set of vectors $\omega = (\omega_1, \omega_2)$ satisfying the Diophantine condition (2.7) for the case $n = 2$: the set consists of the union of closed half lines (or "hairs"). The set of vectors intersects the unit circle in a Cantor set of positive measure.

2.2. The Quasi-periodic Saddle-node

In the general "dissipative" setting we consider the case where (2.3) undergoes a saddle-node bifurcation. Here the center manifold of (2.3) is the (z, λ)–plane. At the moment of bifurcation we have

$$\Omega(0) = 0. \tag{2.4}$$

Moreover, we can obtain the well-known C^∞–format

$$\dot{z} = \mu - cz^2 + \text{hot}\,(z, \mu). \tag{2.5}$$

Recall that if in the equation (2.5) the coefficient c does not vanish, truncation of "hot" gives structurally stable families up to C^0–conjugation [55].

Next we assume that the map

$$\lambda \mapsto (\omega(\lambda), \mu(\lambda)) \tag{2.6}$$

is submersive, a condition coined as BHT-nondegeneracy,[1] compare [4, 14, 17]. For persistence we introduce the following Diophantine condition. Let $\tau > n - 1$ and $\gamma > 0$ be fixed. The condition then reads

$$|\langle \omega, k \rangle| \geqslant \gamma |k|^{-\tau} \text{ for all } k \in \mathbb{Z} \setminus \{0\}. \tag{2.7}$$

In the product of state space and the extended parameter space the Diophantine conditions (2.7) define a nowhere dense set. Here we keep $|z|$ and $|\lambda|$ small and let $\omega \in \mathbb{R}^n$ wander over a suitable domain, keeping the entire set bounded. It has been shown [4] that, for nearly integrable C^∞–small perturbations, when restricted to this Diophantine set, the system (2.2) is structurally stable under Whitney–C^∞ conjugations. One often speaks of quasi-periodic stability.

---

[1] Broer–Huitema–Takens

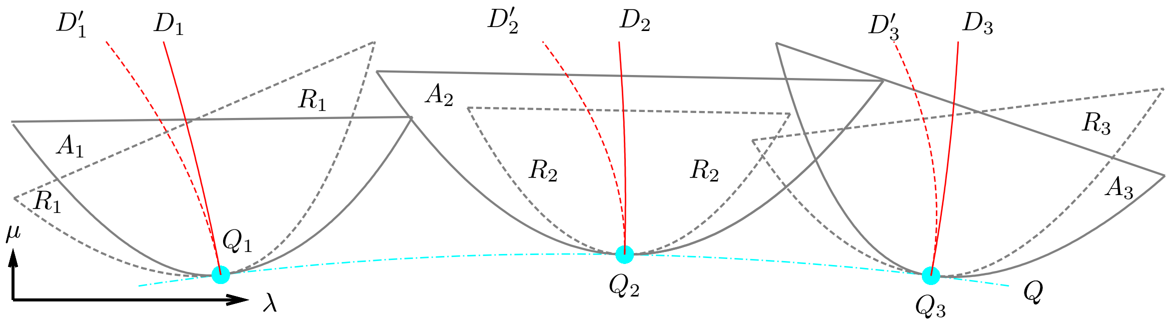

Fig. 2. "Hairs" from Fig. 1 form the uncountable union of lines D_1, D_1', D_2, D_2', D_3, D_3' etc. that carry quasi-periodic dynamics. The lines D_j and D_j' are tangent at Q_j, where the former line refers to attracting and the latter repelling tori. Since this dynamics is ∞-ly normally hyperbolic, these domains can be "fattened" leaving over a countable union of resonance bubbles. The letters A_j and R_j refer attractors and repellors respectively.

Summarizing we can say that the quasi-periodic saddle-node in the center manifold has the following model format

$$\begin{aligned}\dot{x} &= \omega(\lambda) + \mathrm{hot}\,(x,z,\lambda)\\ \dot{z} &= \mu(\lambda) - cz^2 + \mathrm{hot}\,(x,z,\lambda).\end{aligned}$$

For completeness we here also present an analogue for maps $\mathbb{T}^1 \times \mathbb{R} \to \mathbb{T}^1 \times \mathbb{R}$:

$$\begin{pmatrix} x \\ z \end{pmatrix} \mapsto \begin{pmatrix} x + 2\pi\alpha(\lambda) \\ z + \mu(\lambda) - cz^2 \end{pmatrix} + \mathrm{hot}\,(x,z,\lambda). \tag{2.8}$$

2.3. Normal Hyperbolicity

For the integrable approximation the Diophantine condition (2.7) gives rise to a nowhere dense set of positive measure in the parameter space $\mathbb{R}^n \times \mathbb{R} = \{\omega, \mu\}$. By the quasi-periodic stability it follows that a Whitney smooth image of this parametrizes a collection of quasi-periodic invariant n–tori for the original nearly integrable saddle-node system. These tori are r–normally hyperbolic for any $r \in \mathbb{N}$. By [45, Thm. 4.1] this nowhere dense collection of tori can be "fattened" to an open subset of the parameter space. A sophisticated application of the Uniform Contraction Principle [3, 4, 34] leads to an optimal fattening that leaves open only a countable union of small *bubbles* around the resonances given by

$$\mu = 0 \quad \text{and} \quad \langle \omega, k \rangle = 0 \quad \text{for some} \quad k \in \mathbb{Z}.$$

Fig. 2 sketches the structure of the (μ, λ)-parameter space for system (2.8) in the case $s = 1$. A general study of quasi-periodic cuspoid bifurcations was given by [69, 70].

Remarks.

1. It should be said that the dynamics inside the bubbles can be more exciting than quasi-periodic, exhibiting the coexistence of periodicity, quasi-periodicity and chaos. For a case study subordinate to a degenerate Hopf bifurcation we refer to [30–32].

2. The Hamiltonian counterpart is the quasi-periodic Hamiltonian center-saddle bifurcation [39] which has an integrable approximation of the form

$$\begin{aligned}\dot{x} &= \omega + \mathrm{hot}(y,z,\mu)\\ \dot{y} &= 0\\ \dot{z}_1 &= z_2 + \mathrm{hot}(y,z,\mu)\\ \dot{z}_2 &= \mu - z_1^2 + \mathrm{hot}(y,z,\mu).\end{aligned}$$

   In this case no fattening occurs by hyperbolicity, but the "hairs" of Fig. 1 lead to a "Cantorization" of the geometry given by catastrophe theory. For further cases and overviews see [11–14, 41].

2.4. The Quasi-periodic Hopf Bifurcation

We follow the above programme for the case where (2.3) undergoes a Hopf bifurcation. At the moment of bifurcation we have

$$\Omega(0) = \begin{pmatrix} 0 & -\alpha \\ \alpha & 0 \end{pmatrix} \tag{2.9}$$

for $\alpha \in \mathbb{R} \setminus \{0\}$. normalization then leads to another well-known C^∞–format

$$\begin{pmatrix} \dot{z}_1 \\ \dot{z}_2 \end{pmatrix} = \begin{pmatrix} \mu & -\alpha \\ \alpha & \mu \end{pmatrix} \begin{pmatrix} z_1 \\ z_2 \end{pmatrix} - c(z_1^2 + z_2^2) \begin{pmatrix} z_1 \\ z_2 \end{pmatrix} + \mathrm{hot}\,(z, \mu). \tag{2.10}$$

In this case the BHT-nondegeneracy condition requires that the map

$$\lambda \mapsto (\omega(\lambda), \mu(\lambda), \alpha(\lambda)) \tag{2.11}$$

is submersive. Moreover the Diophantine conditions now take the form

$$|\langle \omega, k\rangle + \ell\alpha| \geqslant \gamma |k|^{-\tau} \text{ for all } k \in \mathbb{Z} \setminus \{0\} \text{ and } \ell \in \mathbb{Z} \text{ with } |\ell| \leqslant 4. \tag{2.12}$$

From this, at the level of invariant n–tori, a similar quasi-periodic stability theorem can be derived as for the saddle-node case. The parameter domains with normally hyperbolic n–tori can then be found by an efficient fattening procedure. Also the $(n+1)$–tori are persistent on such a fattened domain. Again the complement of these sets is a countable union of small bubbles around the resonances

$$\mu = 0 \text{ and } \langle \omega, k\rangle + \ell\alpha = 0 \text{ for some } k \in \mathbb{Z} \setminus \{0\} \text{ and } \ell \in \mathbb{Z} \text{ with } |\ell| \leqslant 4.$$

Fig. 3 sketches the structure of the (μ, λ)-parameter space for system (2.10) in the case $s = 1$. Proofs can be found in [3, 4], for overviews see [14, 24, 35]. The skew Hopf bifurcation [23, 25, 27, 65, 72] is an analogue which is not reducible to Floquet form.

2.5. The Hopf–Neĭmark–Sacker Bifurcation

The Hopf–Neĭmark–Sacker bifurcation deals with the intermediate case where a periodic solution bifurcates into an invariant 2–torus when the characteristic exponents cross the complex unit circle. This case can be well studied by a Poincaré map with a bifurcating fixed point, say with derivative

$$\exp \begin{pmatrix} \mu & -2\pi\alpha \\ 2\pi\alpha & \mu \end{pmatrix},$$

where μ passes through 0, see above. Excluding the strong resonances $\alpha = p/q$, with p and q relative prime and $q \leqslant 4$, the diffeomorphism can be shown to have an invariant circle. Its restriction to this circle displays Arnold resonance tongues in a universal setting. For example compare with Fig. 4 displaying a similar array of tongues as these occur in the Arnold family

$$P_{\alpha,\mu} : x \mapsto x + 2\pi\alpha + \mu \sin x \tag{2.13}$$

of circle maps. No further Cantorization occurs in this case. For other descriptions see [14, 24, 35], while for Hamiltonian and reversible counterparts we refer to [7–9, 16].

2.6. Quasi-periodic Period Doubling

On $\mathbb{T}^n \times \mathbb{R} \times \mathbb{R} = \{x, z, \mu\}$ consider the involution

$$I : (x, z, \mu) \mapsto (x_1 + \pi, x_2, \ldots, x_n, -z, \mu), \tag{2.14}$$

assuming the systems (2.1) and (2.2) to be equivariant with respect to I.

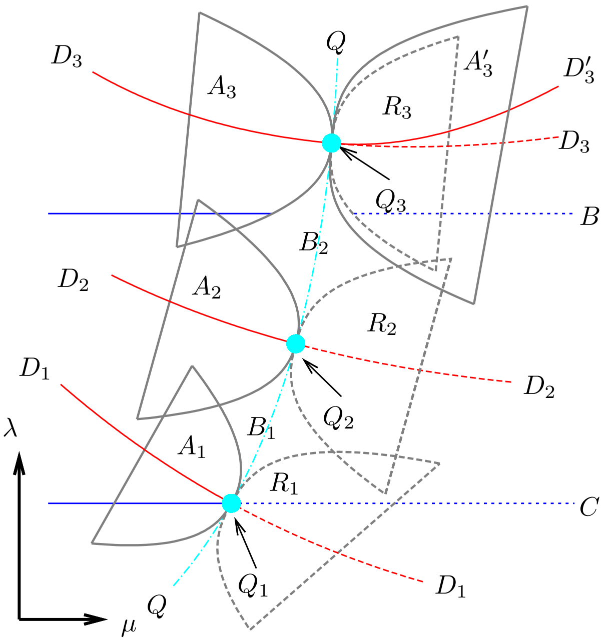

Fig. 3. As in Fig. 2 the "hairs" from Fig. 1 form the uncountable union of lines D_1, D_2, D_3, etc. that carry quasi-periodic dynamics. Since this dynamics is ∞-ly normally hyperbolic, these domains can be "fattened", again leaving over a countable union of resonance bubbles. As before the letters A_j and R_j refer attractors and repellors respectively. On the righthand side there are also domains A'_j, nearly overlapping with R_j, corresponding to the doubled torus attractors, which are Diophantine on 'hairs' D'_j. For clarity only A'_3 and D'_3 have been included in the sketch.

The pitchfork bifurcation

$$\begin{aligned}\dot{x} &= \omega + \ \mathrm{hot}(z^2,\mu) \\ \dot{z} &= z(\mu - z^2) + z\,\mathrm{hot}(z^2,\mu)\end{aligned} \tag{2.15}$$

is persistent in the present I–equivariant setting. This can serve as a double cover for a quotient space obtained from $T^n \times \mathbb{R} \times \mathbb{R}$ by identifying points via

$$(x, z, \mu) \sim I(x, z, \mu).$$

In fact it is much easier to stay on the double cover, keeping track of the deckgroup $\mathbb{Z}_2$ generated by I. Notice that for $n = 1$ this is exactly the well-known Möbius strip, which also forms the natural setting for the standard period doubling of limit cycles. The above applies mutatis mutandis [4, 17], where Cantorization and fattening is according to Fig. 3. For more general studies on a q–fold subharmonic bifurcations see [10, 14, 15, 26]; then the deckgroup equals $\mathbb{Z}_q$.

3. ALGORITHMS

3.1. Newton Algorithm for an Invariant Circle with Fixed Rotation Number

Quasi-periodic bifurcations of invariant circles are here computed by Fourier-based numerical continuation and analysis of normal behavior. We follow [28, 29, 47], see [36, 37, 42–44, 54, 60, 63, 64] for alternative methods. Let $f : \mathbb{R}^n \to \mathbb{R}^n$ be a diffeomorphism and let $\mathbb{T}^1 = \mathbb{R}/2\pi\mathbb{Z}$ denote the unit circle. An invariant circle with rotation number ρ is represented by a parametrization $\gamma : \mathbb{T}^1 \to \mathbb{R}^n$ satisfying the invariance equation

$$f(\gamma(\theta)) = \gamma(\theta + \rho) \quad \text{for all} \quad \theta \in \mathbb{T}^1. \tag{3.1}$$

This is written as an equation on the function space $C(\mathbb{T}^1, \mathbb{R}^n) = \{\gamma : \mathbb{T}^1 \to \mathbb{R}^n\}$ of all continuous parametrizations. Define the *transfer operator*:

$$T_\rho : C(\mathbb{T}^1, \mathbb{C}^n) \to C(\mathbb{T}^1, \mathbb{C}^n), \quad T_\rho(\gamma) = \gamma \circ R_\rho, \tag{3.2}$$

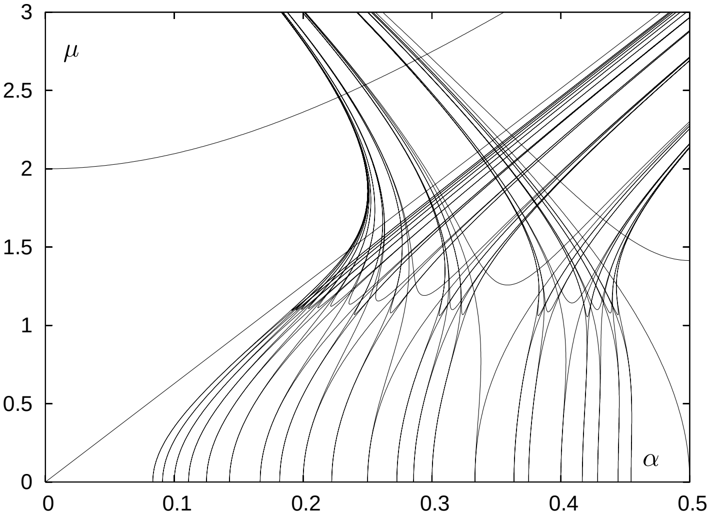

Fig. 4. Resonance tongues in the Arnold family (2.13) of circle maps for $0 \leqslant \alpha \leqslant \frac{1}{2}$. From each point $(\alpha, \mu) = (p/q, 0)$ a tongue emanates, in which the $P_{\alpha,\mu}$ is periodic with rotation number p/q [1, 18, 24]. The boundaries of each tongue are curves of saddle-node bifurcations: moving outward the periodic points annihilate one another pairwise. Note that for $|\mu| \geqslant 1$ the map (2.13) is only endomorphic. The 24 tongues up to $q = 12$ are shown. For $\mu = 1$ the tongues have full measure.

where $R_\rho : \mathbb{T}^1 \to \mathbb{T}^1$ is the rigid rotation of angle ρ, that is $R_\rho(\theta) = \theta + \rho$. Then (3.1) is equivalent to

$$F(\gamma) = 0, \tag{3.3}$$

where F is the functional

$$F : C(\mathbb{T}^1, \mathbb{R}^n) \to \mathbb{R}^n, \quad F(\gamma) = f \circ \gamma - T_\rho(\gamma), \tag{3.4}$$

that is $F(\gamma)(\theta) = f(\gamma(\theta)) - \gamma(\theta + \rho)$ for all $\theta \in \mathbb{T}^1$.

The solution of (3.3) is approximated by discretizing γ as a truncated Fourier series:

$$\gamma_N(\theta) = a_0 + \sum_{k=1}^{N} a_k \cos(k\theta) + b_k \sin(k\theta), \quad a_0, a_k, b_k \in \mathbb{R}^n, \tag{3.5}$$

where N is the truncation order. The unknowns are here the $2N + 1$ Fourier coefficients $a_0, a_k, b_k \in \mathbb{R}^n$. The functional F in (3.4) is discretized by evaluating the image of γ_N at the $(2N + 1)$ mesh points $\theta_j = 2\pi j/(2N + 1) \in \mathbb{T}^1$, $j = 0, \ldots, 2N$: this yields a function F_N of the Fourier coefficients, defined by

$$F_N : \mathbb{R}^{(2N+1)n} \to \mathbb{R}^{(2N+1)n}, \quad (a_0, a_k, b_k)_{k=1}^N \mapsto (f(\gamma_N(\theta_j)) - \gamma_N(\theta_j + \rho))_{j=0}^{2N}. \tag{3.6}$$

A solution of the discretized functional equation $F_N((a_0, a_k, b_k)_{k=1}^N) = 0$ yields an approximation of the invariant circle $\gamma(\theta)$, expressed as a truncated series $\gamma_N(\theta)$ as in (3.5). Zeroes of Eq. (3.6) are found by a Newton algorithm starting from initial values for the Fourier coefficients $(a_0, a_k, b_k)_{k=1}^N$. The differential of F_N around an invariant circle has a one-dimensional kernel, due to the freedom in choosing the origin of θ. This can be dealt with in various ways: for example one may fix $b_1 = 0$ or fix the value of a component of γ_0 (or some other γ_j) at $\theta = 0$.

The normal behavior of a quasi-periodic invariant circle is computed with the method of [47]. Given an invariant circle parametrized by $\gamma(\theta)$, since for $h \in \mathbb{R}^n$ we have

$$f(\gamma(\theta) + h) = f(\gamma(\theta)) + D_x f(\gamma(\theta))h + O(||h||^2), \tag{3.7}$$

the normal linear behavior around $\gamma(\theta)$ is described by the skew-product system

$$(x, \theta) \mapsto (A(\theta)x, \theta + \rho), \tag{3.8}$$

where $A(\theta) = D_x f(\gamma(\theta))$ and $h \in \mathbb{R}^n$. *Reducibility* of the invariant circle is an important property to characterize its normal behavior. Reducibility means that the linearized dynamics around the invariant circle is independent on the angular coordinate along the circle in a suitable coordinate system. A formal definition is now given. The invariant circle parametrized by $\gamma(\theta)$ as in (3.1) is said to be *reducible* if there exists a change of coordinates $x = C(\theta)y$ such that (3.8) becomes

$$(y, \theta) \mapsto (By, \theta + \rho), \tag{3.9}$$

where the matrix $B = C^{-1}(\theta)A(\theta)C(\theta)$ does not depend on θ. Reducibility is a property of the transfer operator defined in (3.2): if the invariant circle is reducible then the normal behavior is fully characterized by the eigenvalues λ of

$$(T_{-\rho} \circ A(\theta))\psi(\theta) = \lambda\psi(\theta), \tag{3.10}$$

see [47]. The idea is to derive finite dimensional approximations for the operators $T_{-\rho}$ and $A(\theta)$. A discretized version A_N of A is given by the Jacobian of the mapping in (3.6). A discretization of T_ρ is the block-diagonal matrix

$$(T_{-\rho} \circ A(\theta))_N, \tag{3.11}$$

where each block is a 2×2 matrix corresponding to rotation of angle $k\rho$: indeed, the rotation $\theta \mapsto \theta + \rho$ applied to the Fourier series in (3.5) is a rotation of angle $k\rho$ on each subspace corresponding to (a_k, b_k). If the circle is reducible to Floquet form, then the eigenvalues of the discretized operator (3.11) provide approximations for the eigenvalues $(\lambda^{\|}, \lambda_1^{\perp}, \ldots, \lambda_{n-1}^{\perp})$ of the matrix B in (3.9): here $\lambda^{\|} = 1$ corresponds to the tangent linear dynamics and $\lambda_j^{\perp}, j = 1, \ldots, n-1$ determine the linear dynamics in the normal directions to the circle.

The numerically computed eigenvalues of (3.11) are sorted according to their estimated error, as described in [47, Sec. 3.2], and the most precise 25% is retained for the following computations. One then aims to identify the number of distinct classes of *ρ-related eigenvalues* in the spectrum of the discretized operator. Two eigenvalues λ_1 and λ_2 are called *ρ-related* (or *related*, for shortness) if there exists $k \in \mathbb{Z}$ such that $\lambda_1 = \exp(ik\rho)\lambda_2$. A signature of reducibility of the normal linear behavior is that the set of eigenvalues partitions into at most n distinct classes of related eigenvalues, where n is the phase space dimension. This means that all the sufficiently precise eigenvalues of the discretized transfer operator belong to circles in the complex plane having radii approximately equal to

$$\left|\lambda^{\|}\right|, \left|\lambda_1^{\perp}\right|, \ldots, \left|\lambda_{n-1}^{\perp}\right|.$$

The logarithms of these radii are the Lyapunov exponents: this provides direct information about the stability of the invariant circle. Examples are given in Section 4.

An alternative method for the computation of quasi-periodic invariant circles (and tori) is the so-called "fractional iteration" method developed by C. Simó in the 1990s. The basic idea is to work in the phase space instead of the Fourier space. A return map is *synthesized* by interpolating points obtained from different (integer) powers of the initial map (or suitable Poincaré iterates in the case of flows). Once again, one looks for invariant circles which have "sufficiently Diophantine" rotation number ω. Denoting by $T = 2\pi/\omega$ the "period" of the invariant circle, one can use the interpolation procedure sketched above to define the T-th iterate of the map f: note that $T \notin \mathbb{Q}$, since ω is Diophantine, hence the name of "fractional iteration". A modified Newton method is then used to find zeroes of the equation $f^T(x) - x = 0$. The solution to this equation is a single point on the invariant circle.

The fractional iteration method was applied to the three-dimensional restricted three-body problem in [63, 64]. This method in general works well for stable or elliptic tori. In case of instability, a parallel shooting strategy can be adopted, see [28, 29] for a broader discussion and a comparison with the Fourier-based method. The applicability of the method can be fully justified if we assume that the tori are sufficiently regular and the linearized dynamics around them is reducible. An important advantage of the fractional iteration method with respect to Fourier-based methods is the applicability to high dimensional cases: indeed, the method has been also applied successfully to the computation of 2D invariant tori for PDE [59] with a moderate computational effort. However, both the fractional iteration and the Fourier-based methods "suffer" in the case of resonant or near-resonant dynamics.

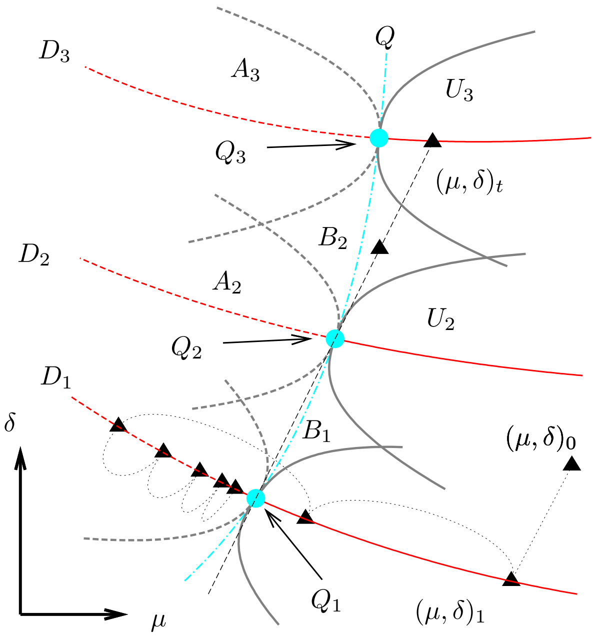

Fig. 5. Sketch of the structure of the parameter plane for a quasi-periodic period doubling of an invariant circle of a map depending on two parameters (μ, δ), based on the quasi-periodic bifurcation theory of Section 2.

3.2. General Strategy for Numerical Continuation of Invariant Circles

We consider a map $G_{\mu,\delta}$ depending on two real parameters (μ, δ). To start with, suppose that the map $G_{\mu,\delta}$ exhibits quasi-periodic period-doubling bifurcations where an invariant circle attractor loses stability and a "doubled" circle attractor branches off, compare with Section 2.6. Generically we expect that the (μ, δ)-parameter plane is *Cantorized* near the bifurcation: a Cantor-like foliation by curves is expected to occur in the parameter plane, such that the bifurcating invariant circle has quasi-periodic dynamics (satisfying a Diophantine condition like (2.7)) for all parameter values on the Cantor-like foliation. The rotation number of the invariant circle is fixed to a single irrational value when parameters vary on a single curve in the Cantor-like foliation. Each of these curves is a *quasi-periodic "hair"* [20, 68], compare with Section 2.

The conceptual sketch in Fig. 5 illustrates the theoretical expectation for the Cantor-like structure near a quasi-periodic period doubling bifurcation. An invariant circle $\mathscr{C}$ with Diophantine rotation number occurs for (μ, δ) on the "hairs" $D_1, D_2, \ldots$ The "fattening" procedure of Section 2.3 yields so-called *flat discs* A_j and U_j in the parameter plane, such that the invariant circle $\mathscr{C}$ is attracting for parameters in A_j, unstable for parameters in U_j and normally hyperbolic for parameters in the union $A_j \cup U_j$. A doubled invariant circle attractor $\mathscr{C}_2$ exists for parameters in $U_1, U_2, U_3, \ldots$. The tangency points Q_j of disks U_j and A_j form a *frayed* (Cantorized) bifurcation boundary P. A frayed boundary can be thought of as a Cantor set, contained inside a *virtual curve* (denoted as Q in Figs. 2, 3, and 5), the gaps of which are filled up with resonance "bubbles".

The theory does not specify the dynamics inside the resonance "bubbles" B_k: there we expect intricate structures of bifurcations of periodic orbits. Indeed, a cascade-like structure of subordinate quasi-periodic bifurcations was found in [21, 22] for the quasi-periodic Hopf bifurcation.

Quasi-periodic period doubling bifurcations admit a simple description if the bifurcating invariant circle is reducible [44, 47, 49] and if parameters are restricted to move along a single Diophantine "hair" D_j in the two-dimensional parameter space. In this case, one of the normal eigenvalues of the circle $\mathscr{C}$ becomes -1 at a single point along the "hair" D_j: this is the tangency point Q_j between two discs A_j and U_j, see [4] and compare with the "Invariant Curve Theorem" of [46]. At that moment, $\mathscr{C}$ turns unstable and a doubled circle attractor $2\mathscr{C}$ shows up. This may occur in two ways [33, 51]:

1. the circle $2\mathscr{C}$ consists of a single connected curve, which is roughly twice as "long" as the bifurcating circle $\mathscr{C}$; in this case the rotation number of $2\mathscr{C}$ is halved with respect to the rotation number of the bifurcating circle $\mathscr{C}$ (near the bifurcation point) and the center manifold of the bifurcation is a Möbius strip;

2. the circle $2\mathscr{C}$ consists of a pair of connected curves, which are mapped onto another by G (a so-called periodically invariant circle); in this case, the rotation number of G^2 is the same as the rotation number of the bifurcating circle $\mathscr{C}$ (near the bifurcation point) and the center manifold of the bifurcation is a cylinder.

The Newton method described in Section 3.1 can be applied to map $G_{\mu,\delta}$ to numerically compute the invariant circle $\mathscr{C}$. In the simplest version, one can thereby refine an initial approximation of the Fourier coefficients of $\mathscr{C}$ for **fixed values of the parameters** (μ, δ), for which the rotation number ρ of $\mathscr{C}$ is known and is irrational. If the rotation number is not known, a modified Newton algorithm [62] is used to refine initial approximations for both the Fourier coefficients and ρ. In this way, one is constraining the Newton algorithm to a single point along a quasi-periodic "hair". Fig. 5 illustrates this initial process: the starting parameter pair $(\mu, \delta)_0$ converges to $(\mu, \delta)_1 \in D_1$ by application of the modified Newton algorithm.

Parameters can be "slided" along a quasi-periodic "hair" D_j by using a modified Newton algorithm which refines both the Fourier coefficients and the values (μ, δ), **but leaves ρ fixed to the same irrational value**. In our experience, this is the most effective strategy, as the good arithmetical properties of the Diophantine rotation numbers usually ensure much faster decay of the Fourier coefficients than for (nearly)-resonant rotation numbers. This suggests the following algorithm.

Algorithm 1: numerical continuation of quasi-periodic invariant circles.

1. Find an invariant circle $\mathscr{C}_{\rho_0}$ for initial parameter values $(\mu, \delta)_0$ and compute a numerical approximation for its rotation number ρ_0.

   For example, $\mathscr{C}_{\rho_0}$ may be found by forward iteration if it is attractive, or by analytical means for specific parameter values. Approximations for ρ_0 can be computed as described in e.g. [68, Appendix B].

2. Compute a numerical approximation for the Fourier coefficients of $\mathscr{C}_{\rho_0}$.

   This may be obtained by sorting the points of an orbit on $\mathscr{C}_{\rho_0}$, interpolating them on a regular grid with respect to an angular variable and computing the Fourier coefficients by numerical integration using the interpolated points.

3. Compute refined approximations $\mathscr{C}_{\rho_1}$ and ρ_1 using a modified Newton method.

   This will usually move the parameters onto values $(\mu, \delta)_1$ on a Diophantine "hair".

4. Predict the Fourier coefficients of a new invariant circle for parameter values $(\mu, \delta)_{j+1}$ from the invariant circle occurring at $(\mu, \delta)_j$.

   This prediction step is performed according to standard extrapolation techniques, e.g. using a Lagrange polynomial [62] interpolating the Fourier coefficients and parameter values of the last 2–4 computed invariant circles.

5. Refine the predicted invariant circle by a modified Newton method that leaves the rotation number **fixed**.

Re-iteration of steps 4 and 5 yields an approximation for the quasi-periodic "hair" D_1, corresponding to rotation number ρ_1, as a finite set of parameter pairs $\{(\mu^k_{\rho_1}, \delta^k_{\rho_1}) \mid k = 1, 2, \ldots\}$ and corresponding Fourier coefficients. Steps 4 and 5 above form a usual predictor-corrector approach for numerical continuation of invariant objects, with the only *caveat* that the rotation number is constrained to remain fixed at the initial (Diophantine) value ρ_1. This approach avoids the problems due to the (generically) non-smooth dependence of the rotation number on the parameters. Algorithm 1 forms the basis for our general strategy to compute quasi-periodic bifurcations.

Algorithm 2: numerical continuation of quasi-periodic bifurcations of an invariant circle.

1. Perform initial steps 1–3 of Algorithm 1.
2. During iteration of steps 4–5 of Algorithm 1, monitor a test function to detect crossing of the single bifurcation point Q_{ρ_1} along "hair" D_1.

   This requires computing the normal behavior of $\mathscr{C}_{\rho_1}$ using the method of Section 3.1. For the quasi-periodic period doubling we use the test functions $f_1 = \lambda_1^{\perp} + 1$ and $f_2 = \lambda_2^{\perp} + 1$ to check that one of the eigenvalues crosses -1 along the real line in the complex plane.
3. If a test function crosses zero, compute a precise approximation for the quasi-periodic bifurcation point Q_1.

   We compute zeroes of the test functions $f_1(s)$ or $f_2(s)$ by a secant search on the pseudo-arc length s along the continuation path on "hair" D_1.
4. Use a predictor step to compute a new approximate value of parameters, rotation number and Fourier coefficients at another quasi-periodic bifurcation and repeat the above steps.

Again, iteration of steps 3–4 of amounts to a usual prediction-correction approach, with the following important *caveats*.

Assume that quasi-periodic bifurcation points Q_1 and Q_2 have been computed by Algorithm 2. A predictor step for Q_3 can then be obtained by linear extrapolation, as shown in Fig. 5. If the predictor "lands" on a Diophantine "hair" (e.g. $(\mu, \delta)_t \in D_3$ for Fig. 5), then the continuation procedure of Algorithm 1 can be started. The problem in our setting is that there is only a **positive probability** that the predicted parameter values will "land" on a Diophantine "hair". There is also **positive probability** that the predictor will fall within a "bubble" (e.g. B_2 for Fig. 5) where the invariant circle may no longer exist. This is sketched by the predicted point falling in B_2 in Fig. 5.

Problems also arise if the predictor falls inside a resonance "gap" (not necessarily a "bubble"): in this case, indeed, (3.1) does not hold, because the dynamics on the invariant circle is of Morse–Smale type. In other words, we are in the interior of a resonance "tongue" (compare Fig. 4), where the invariant circle is no longer analytic but only finitely differentiable, see e.g. [18, Sec. 3.1]. Hence the Fourier coefficients decay slowly and the Newton method of Section 3.1 breaks down.

To prevent the above problems, the prediction step 3 is the only place where the rotation number is allowed to vary in Algorithm 2: the ensuing correction is performed with fixed ρ. In this way, one can ensure that the predicted ρ is Diophantine. Indeed, given a predicted value $\widehat{\rho}$, one can simply change the continued fraction expansion of $\widehat{\rho}$ by adding a small correction as follows: first we add a large quotient (so that the corrected number will be rather close to the initial $\widehat{\rho}$) and then a tail like the golden mean. The number ρ thus obtained is a *noble number* and, hence, Diophantine. This is the most sensitive part in the algorithm: the "fumbling" in parameter space in search of "sufficiently irrational" rotation numbers, trying to "dodge" resonance gaps and "bubbles".

4. EXAMPLE 1: A MODEL MAP FOR THE HOPF-SADDLE-NODE BIFURCATION OF FIXED POINTS

We consider the following map:

$$G : \begin{pmatrix} w \\ z \end{pmatrix} \mapsto \begin{pmatrix} e^{i(\omega_0+\gamma\delta)} w[1 - \gamma(\gamma\mu + az + \gamma z^2)] \\ z + \gamma(1 - |w|^2 - z^2) \end{pmatrix} + \begin{pmatrix} \gamma^3(\varepsilon_1 \overline{w}^4 + \varepsilon_2 z^4) \\ 0 \end{pmatrix}, \tag{4.1}$$

where $w = x + iy \in \mathbb{C}$, $z \in \mathbb{R}$ and $a = a_1 + ia_2 \in \mathbb{C}$. Map (4.1) was constructed in [21] as a model to study the Hopf-saddle-node (HSN) bifurcation for fixed points of 3D diffeomorphisms. The HSN bifurcation occurs when the eigenvalues of the derivative at the fixed point are

$$e^{i\omega_0}, e^{-i\omega_0} \text{ and } 1, \tag{4.2}$$

subject to the non-resonance conditions

$$e^{in\omega_0} \neq 1 \text{ for } n = 1, 2, 3, 4, \tag{4.3}$$

and to generic requirements on the higher-order terms and on the parameter dependence [21, Lemma 6]. Map (4.1) was constructed to study the dynamics near a $1:5$ resonance of the complex conjugate eigenvalues, corresponding to $\omega_0 = 2\pi/5$. This resonance was chosen because it has the lowest order among the weak resonances, and therefore it is likely to have a most visible influence on the bifurcation diagram. As in [21, 68] we use (μ, δ) as control parameters and fix $\gamma = 0.1$, $\varepsilon_1 = \varepsilon_2 = 1$, $a_1 = -1$, $a_2 = 1/\sqrt{2}$, see [67, App. 4E] for our choice of these coefficients.

Model map (4.1) is obtained by perturbing the flow of a truncated normal form for the Hopf-saddle-node of equilibria of vector fields. As such, it exhibits quasi-periodic Hopf bifurcations which are "inherited" by construction from the unperturbed vector field, see [21, 67]. As it turns out, map (4.1) also exhibits quasi-periodic period doubling and saddle-node bifurcations of invariant circles. These three bifurcation types are presented in the next sections, to illustrate the theory of Section 2 and algorithm of Section 3.

4.1. Quasi-periodic Hopf Bifurcations

An invariant circle attractor of map (4.1) loses normal hyperbolicity (stability) as G decreases. Thereby, the invariant circle turns into a repellor and an invariant 2-torus attractor branches off. This process is illustrated in Fig. 6: the top row shows the invariant circle for three values of (μ, δ), corresponding to an attractor, a weak attractor (very close to the quasi-periodic bifurcation) and a repellor surrounded by the 2-torus attractor. The invariant circle is analytic in all cases, as indicated by the decay of the modulus of the Fourier coefficients as a function of the wavenumber k. In this case we used $N = 100$ for the order of the Fourier truncation in (3.5).

The bottom row of Fig. 6 illustrates the normal behavior of the invariant circles in the top row. In each case, our algorithm indicates that the circle is reducible, since the eigenvalues of the discretized transfer operator (3.11) all lie on circles in the complex plane. Specifically, following the approach of [47], we checked that the 25% most precise eigenvalues belong – with sufficient accuracy – to circles in the complex plane. The logarithms of the radii of these "circles of eigenvalues" are the Lyapunov exponents of the invariant circles, see Section 3.1. In all cases, for the eigenvalues $(\lambda^{\|}, \lambda_1^{\perp}, \lambda_2^{\perp})$ we observe numerically that:

$\lambda^{\|} = 1$: corresponding to the tangent direction along the invariant circle;

$\lambda_1^{\perp} = \overline{\lambda_2^{\perp}}$: the two normal eigenvalues are complex conjugate, corresponding to dynamics of focus type in the normal direction.

Tab. 1 shows the first 13 numerically computed eigenvalues of the discretized transfer operator (3.11) for the invariant circle of Fig. 6 left. The algorithm identifies two classes of related eigenvalues: one class corresponding to $\lambda^{\|}$ and just one class corresponding to both $\lambda_{1,2}^{\perp}$. In this case, the Lyapunov exponents are $\chi_1 = \log \lambda^{\|} = 0$ and $\chi_{2,3} = \log(|\lambda_{1,2}^{\perp}|) < 0$. For the right column of Fig. 6, repulsivity of the invariant circle is identified by one circle of eigenvalues outside the unit circle: this corresponds to a pair of positive Lyapunov exponents.

According to the theory of Section 2, quasi-periodic bifurcations of invariant circles admit a simple dynamical description when the parameters are constrained to vary on the set where the rotation number on the invariant circle is fixed to an irrational (Diophantine) value. This set is (locally) a curve and the collection of all such curves forms a Cantor-like foliation by quasi-periodic "hairs" in the parameter plane. Quasi-periodic bifurcations occur on points along the "hairs" which are isolated (if the bifurcations are nondegenerate) and form a frayed boundary in parameter space. This frayed boundary is interrupted by "bubbles" corresponding to internal or normal-internal resonances on the bifurcating invariant circles.

Fig. 7 left provides an illustration of the Cantor-like foliation in the (μ, δ)-parameter plane corresponding to the quasi-periodic Hopf bifurcations of map G. The dots along the quasi-periodic "hairs" mark the points where the circle of eigenvalues corresponding to $\lambda_{1,2}^{\perp}$ crosses the unit circle, compare with Fig. 6 center. All three Lyapunov exponents vanish at such points. This is illustrated

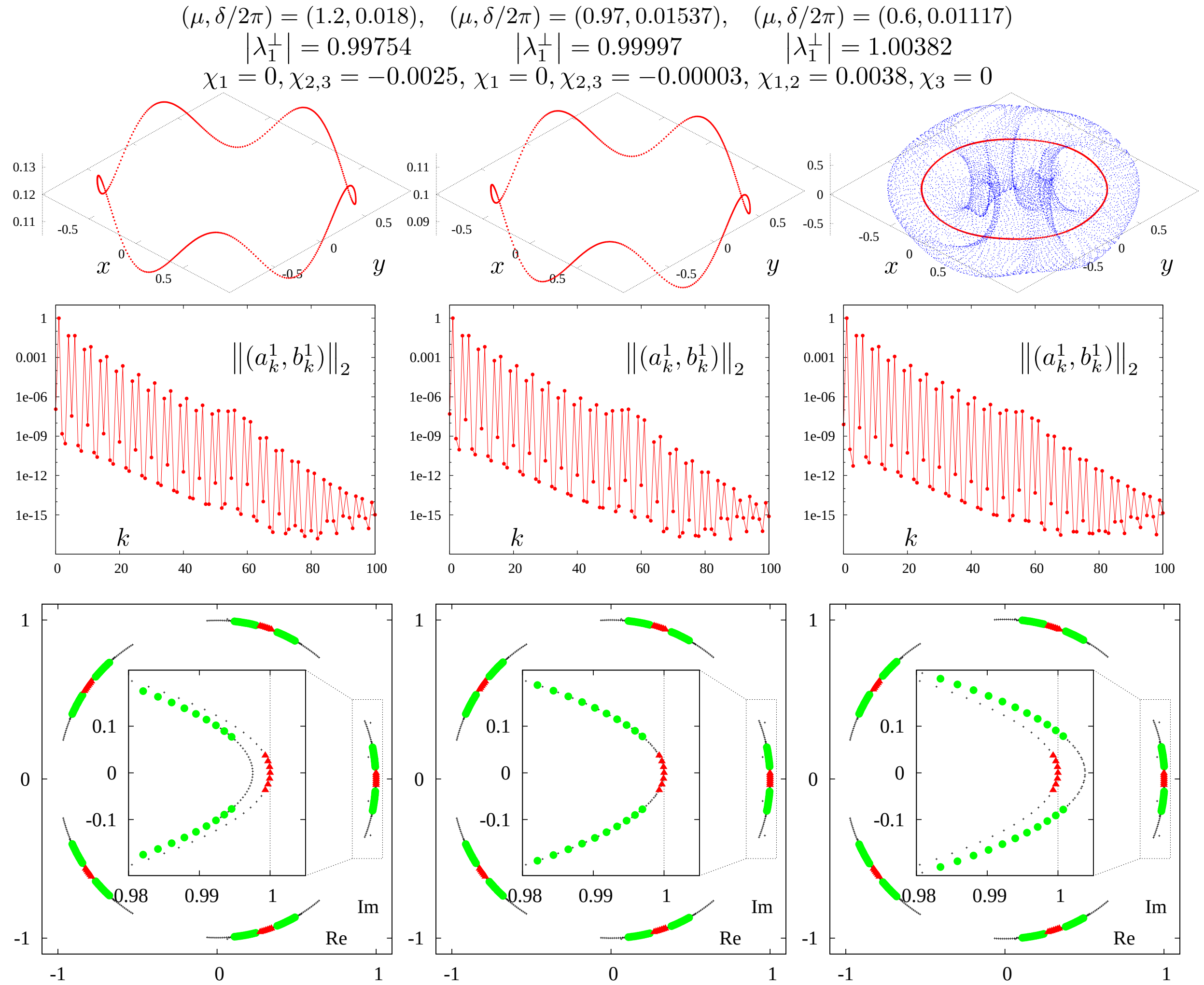

$(\mu, \delta/2\pi) = (1.2, 0.018)$, $(\mu, \delta/2\pi) = (0.97, 0.01537)$, $(\mu, \delta/2\pi) = (0.6, 0.01117)$

$\left|\lambda_1^{\perp}\right| = 0.99754$ $\left|\lambda_1^{\perp}\right| = 0.99997$ $\left|\lambda_1^{\perp}\right| = 1.00382$

$\chi_1 = 0, \chi_{2,3} = -0.0025$, $\chi_1 = 0, \chi_{2,3} = -0.00003$, $\chi_{1,2} = 0.0038, \chi_3 = 0$

Fig. 6. Illustration of an invariant circle of the map G (4.1), undergoing a quasi-periodic Hopf bifurcation. Top row: invariant circle for three values of $(\mu, \delta/2\pi)$ (indicated on top of each panel), with rotation number fixed to $\rho = 0.200393786271967$. Left & middle: attracting circle. Right: repelling circle coexisting with a 2-torus attractor. In all 3 cases, the normal eigenvalues are complex conjugate: $\lambda_1^{\perp} = \overline{\lambda_2^{\perp}}$. Modulus $\left|\lambda_1^{\perp}\right|$ and related Lyapunov exponents $\chi_1 \geqslant \chi_2 \geqslant \chi_3$ are indicated on top of each panel. Middle row: modulus $\left\|(a_k^1, b_k^1)\right\|_2$ of the Fourier coefficients of the x-component of the parametrization of the invariant circle on top as a function of k. Bottom row: eigenvalues of the discretized transfer operator (3.11) in $\mathbb{C}$. The magnification in the inset illustrates the existence of two classes of related eigenvalues of (3.11), corresponding to two separate circles in $\mathbb{C}$. Eigenvalues which our algorithm identifies as sufficiently precise are plotted with either thick dots (green) or triangles (red), according to which of the two classes they are assigned to. The remaining ones are plotted in black. The triangles (red) denote the class of the unit eigenvalue in the tangent direction.

in Fig. 8 left, showing the Lyapunov exponents as a function of μ varying along the horizontal line labelled B in Fig. 7 left.

The rotation number ρ along line B is also shown in Fig. 8 left. The rotation number is constant and equal to 0.2 for large μ: this corresponds to a 1:5 resonance "gap" where the invariant circle is phase-locked to a pair of period five orbits, an attractor and a saddle, see Fig. 9a. Such resonant invariant circles are only finitely differentiable and the algorithm of Section 3.1 breaks down, as discussed in Section 3.2. By decreasing μ, the circle exits the 1:5 resonance gap and the rotation number begins to increase (Fig. 8 left). Generically, one expects the graph of the rotation number to be a *devil's staircase* [38], where:

resonances on the invariant circle are dense in μ, corresponding to *plateaus* of constant rotation number;

Table 1. First 13 eigenvalues (out of a total of 603) of the discretized transfer operator (3.11) for the invariant circle of Fig. 6 (top left panel) with $N = 100$, sorted as described in Section 3.1. Two classes are identified, corresponding to two distinct circles in the complex plane, see Fig. 6 (bottom left panel). Class 0 corresponds to a pair of complex conjugate eigenvalues with modulus approximately 0.99754 and class 2 corresponds to the (unit) real eigenvalue in the tangent direction.

Modulus	Argument		class
0.9975425183436066	0.1392935712802970	4.963e+00	0
0.9975425183436066	-0.1392935712802970	4.963e+00	0
0.9975425183436070	1.1198177222738102	5.497e+00	0
0.9975425183436070	-1.1198177222738102	5.497e+00	0
0.9975425183436107	1.3984048648344078	5.642e+00	0
0.9975425183436107	-1.3984048648344078	5.642e+00	0
0.9975425183436095	-0.7626636377618755	7.030e+00	0
0.9975425183436095	0.7626636377618755	7.030e+00	0
0.9975425183436051	-0.4840764952012779	7.321e+00	0
0.9975425183436051	0.4840764952012779	7.321e+00	0
0.9999999999999969	0.0000000000000000	8.133e+00	2
0.9975425183436020	-0.4964476557922389	9.174e+00	0
0.9975425183436020	0.4964476557922389	9.174e+00	0

Table 2. Legend of the color coding for Fig. 7 right panel: the attractors are classified by means of the Lyapunov exponents (χ_1, χ_2, χ_3). If printed in grey tones, the most abundant domains (black, dark blue, green and pale blue) are seen as black, dark grey, grey and pale grey, respectively.

color	Lyapunov exponents	attractor type
red	$\chi_1 > 0 = \chi_2 > \chi_3$	strange attractor
yellow	$\chi_1 > 0 > \chi_2 > \chi_3$	strange attractor
blue	$\chi_1 = 0 > \chi_2 = \chi_3$	invariant circle of focus type
green	$\chi_1 = \chi_2 = 0 > \chi_3$	invariant two-torus
black	$\chi_1 = 0 > \chi_2 > \chi_3$	invariant circle of node type
grey	$0 > \chi_1 > \chi_2 = \chi_3$	periodic point of focus type
pale blue	$0 > \chi_1 = \chi_2 \geqslant \chi_3$	periodic point of focus type
magenta	$0 > \chi_1 > \chi_2 > \chi_3$	periodic point of node type
white		no attractor detected

quasi-periodic dynamics occurs for a positive Lebesgue measure nowhere dense set of μ-parameter values.

For the case of Fig. 8 left, we did not identify other resonance *plateaus*: they might be of very small size, possibly below numerical resolution of standard double precision.

In the 1:5 resonance gap of Fig. 8 left, all Lyapunov exponents are negative: this corresponds to a periodic attractor P^5_-, see Fig. 9a. This periodic attractor is of focus type in the μ-interval where

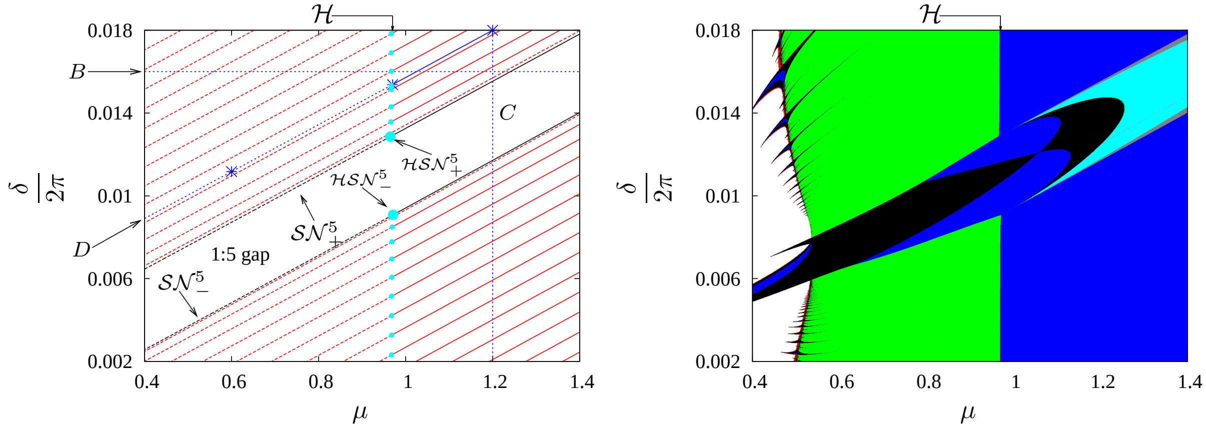

Fig. 7. Left: Cantor-like foliation of curves (red) in the $(\mu, \delta/2\pi)$ parameter plane where the invariant circle of Fig. 6 has a fixed irrational rotation number ρ and is stable (solid) or unstable (dashed). The difference in rotation number between any two consecutive curves is about 0.0001 (except, of course, for the 1:5 gap). Thick dots (cyan): quasi-periodic Hopf bifurcations on frayed boundary $\mathcal{H}$. Black: curves of $\mathcal{SN}^5_\pm$ of saddle-node bifurcations of period 5 points. Asterisks: the three pairs of parameter values of Fig. 6 (left, middle, right column), belonging to "hair" D defined by $\rho = 0.200393786271967$ constant on the invariant circle. See Fig. 8 below for the meaning of the lines B and C. Right: Lyapunov diagram of the map G near the intersection of the 1:5 resonance gap with the frayed boundary $\mathcal{H}$ of quasi-periodic Hopf bifurcations, see Tab. 2 for the color coding.

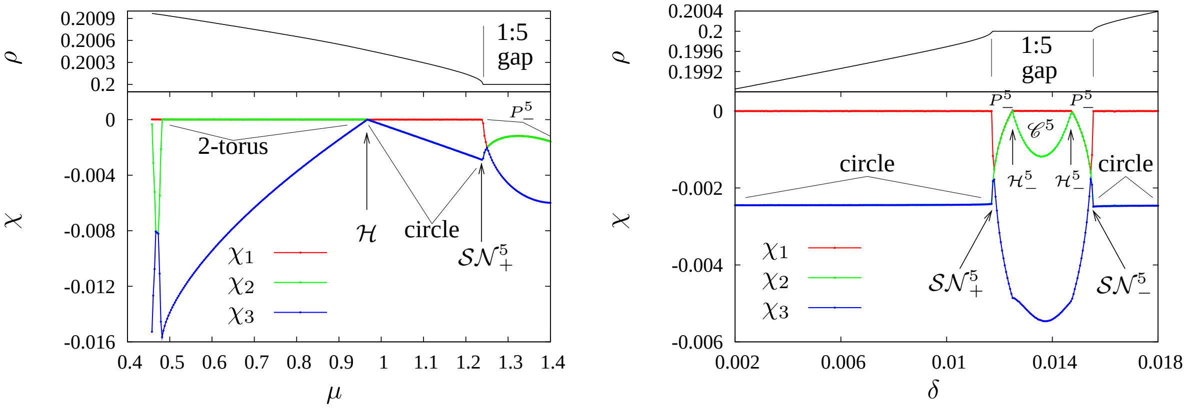

Fig. 8. Left: Lyapunov exponents $\chi_1 \geqslant \chi_2 \geqslant \chi_3$ (bottom part of the panel) and rotation number ρ around the origin (top part) as a function of μ for fixed $\delta/2\pi = 0.016$, that is along the horizontal dotted line labelled B in Fig. 7 left. Right: same as left for fixed $\mu = 1.2$ and varying δ, that is along the vertical dotted line labelled C in Fig. 7 left.

$\chi_1 = \chi_2$ and is of node type near the edge of the resonance gap. The maximal Lyapunov exponent χ_1 vanishes at the edge of the gap: this corresponds to a saddle-node bifurcation of period 5 points, where the attractor P^5_- collapses with the saddle P^5_+ (see Fig. 9a) and they both disappear. This occurs on bifurcation curve $\mathcal{SN}^5_+$ which, together with saddle-node bifurcation curve $\mathcal{SN}^5_-$, forms the edges of the 1:5 resonance gap, see Fig. 7 left. Both $\mathcal{SN}^5_\pm$ are roughly parallel to the Diophantine "hairs": the curves of this Cantor foliation "accumulate" with a square-root asymptotics onto the edges $\mathcal{SN}^5_\pm$ of the 1:5 resonance gap.

The 1:5 gap "intersects" the frayed boundary $\mathcal{H}$ of quasi-periodic Hopf bifurcations at a 1:5 internal resonance "bubble". The main goal of [21] was to study this "bubble" using model G, which was constructed *ad-hoc*. Generically, one expects a dense set of such "gaps" and "bubbles" but, as mentioned above, the size of the other resonances in the parameter plane seems very small in this case.

All three Lyapunov exponents vanish at a single point on curve B (Fig. 8 left): this is where

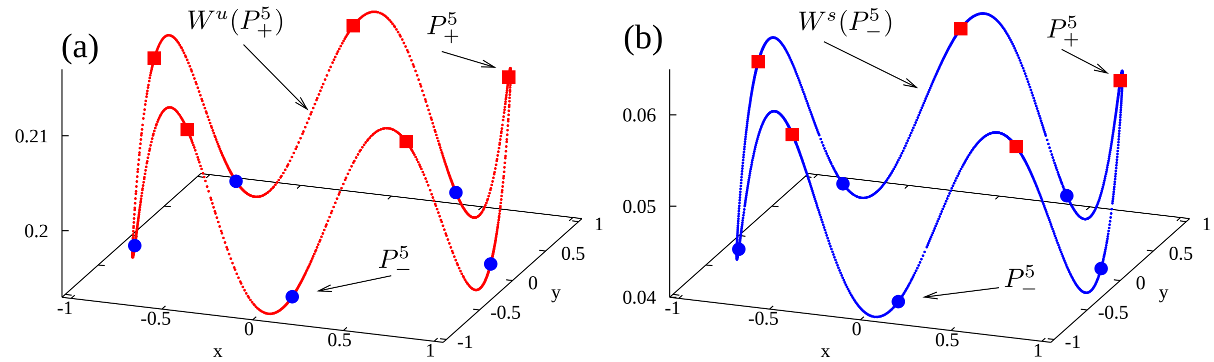

Fig. 9. (a) The 1:5-resonant attracting invariant circle $\mathscr{C}$ is formed as the union of the unstable manifold $W^u(P^5_+)$ (red) with the node-focus attractor P^5_- (blue dots), where P^5_+ (red squares) is a saddle-focus. (b) The 1:5-resonant repelling circle $\mathscr{C}$ is formed by the union of the stable manifold $W^u(P^5_-)$ (blue) with the node-focus repellor P^5_+ (red squares), where P^5_- (blue dots) is a saddle-focus. In both cases, parameters lie within the 1:5 resonance gap and outside the elliptic closed domain bounded by the Hopf bifurcation curve labelled $\mathcal{H}^5$ in Fig. 7 right. For (a) and (b) parameters lie respectively at the right and at the left of the frayed quasi-periodic Hopf boundary $\mathcal{H}$.

the quasi-periodic Hopf bifurcation takes place. Of course, we cannot state this with certainty: horizontal lines such as B hit a "good" parameter value (in the terminology of [30, 46]) with positive probability, but there is also positive probability that they hit a "bubble". The thick dots of Fig. 7 left belong to the frayed Hopf boundary $\mathcal{H}$: they are identified by performing continuation for *fixed rotation number*, varying (μ, δ), and looking for (μ, δ) values where the three Lyapunov exponents vanish, or equivalently, the "inner" circle of eigenvalues of the discretized transfer operator crosses the unit circle as in Fig. 6 bottom.

The Lyapunov exponents provide a powerful tool to characterize the dynamics. Several features discussed above can be recognized in the Lyapunov diagram of Fig. 7 right. The circle is attracting and quasi-periodic in the blue domain at the right of Fig. 7 right, where it is of focus type in the normal direction, see Tab. 2. The quasi-periodic frayed Hopf boundary $\mathcal{H}$ is identified as separating the blue from the green parameter domain: in the latter domain, a 2-torus attractor occurs. This is identified by two vanishing Lyapnov exponents, compare with Fig. 8 left. At the right of $\mathcal{H}$, the 1:5 resonance gap is identified in Fig. 7 right as a pale blue strip with grey edges matching the two saddle-node bifurcation curves $\mathcal{SN}^5_\pm$ of Fig. 7 left. The resonance gaps of Fig. 7 left and right do not match at the left of $\mathcal{H}$, because the invariant circle has turned into a repellor in that region (see Fig. 9b), whereas the Lyapunov diagram can only inform us about the attractors.

Additional bifurcations occur at the 1:5 "bubble" near $\mathcal{H}$. The period 5 orbit P^5_- of Fig. 9a loses stability at a Hopf bifurcation of periodic points. The invariant circle is therefore broken by loss of normal hyperbolicity: the unstable manifold $W^u(P^5_+)$ no longer connects with P^5_- after the loss of stability, see Fig. 10a. The stable manifold of P^5_- approaches P^5_+, but then escapes, see Fig. 10b. A periodically invariant circle attractor, $\mathscr{C}^5$, branches off from P^5_- at the Hopf bifurcation: $\mathscr{C}^5$ consists of five circles mapped onto each other by the map G (only one of the five circles is shown in Fig. 10a). The black lobe of the Lyapunov diagram Fig. 7 right within the 1:5 resonance gap is explained by the presence of $\mathscr{C}^5$, which is of node type near its branching from P^5_-. This is also visible in Fig. 8 right, showing the Lyapunov exponents as a function of δ varying along line C of Fig. 7 left. The rotation number around the origin has a horizontal plateau on an interval of δ corresponding to the 1:5 resonance. However, the maximal Lyapunov exponent becomes zero for a sub-interval corresponding to the presence of $\mathscr{C}^5$, which is of node type since $\chi_2 \neq \chi_3$.

A rather complex bifurcation structure occurs within the 1:5 "bubble" near $\mathcal{H}$, related to secondary quasi-periodic bifurcations of the period 5 invariant circle $\mathscr{C}^5$. This was described in [21], to which we refer the reader for details. Suffice here to say, that, by the genericity of the construction of our model map, the same level of complexity is expected near *any* resonance "bubble" along frayed boundaries of quasi-periodic Hopf bifurcations. The ubiquitous presence of

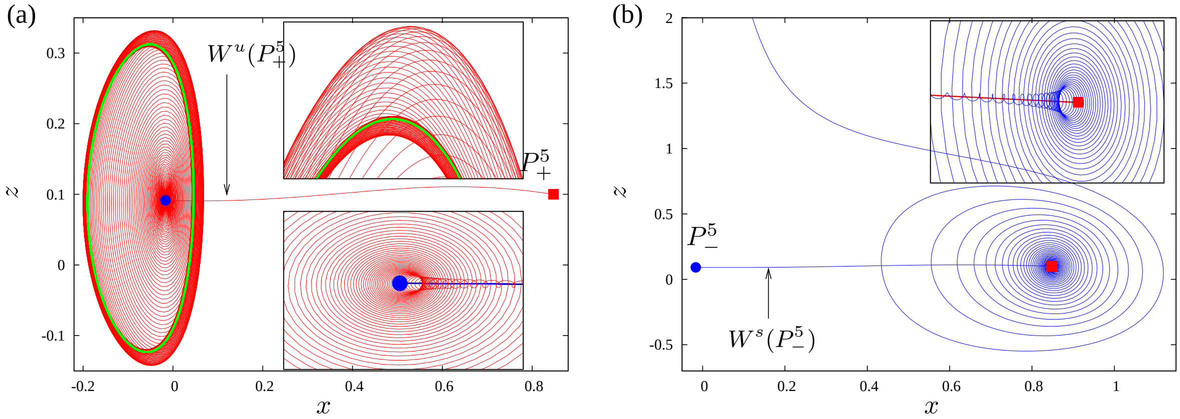

Fig. 10. (a) Projection on (x, z) of the points P^5_- (blue dot) and P^5_+ (red square), with one branch of the 1D unstable manifold $W^u(P^5_+)$ (red) and with the period five circle attractor $\mathscr{C}^5$ (green). The fifth iterate G^5 is used for the computations, so that only one "fifth" of the whole phase portrait is shown. Magnification of a neighborhood of P^5_- is given in the lower box, where a portion of $W^s(P^5_-)$ is added (blue). The upper box contains a magnification of the "scrolls" of $W^u(P^5_+)$ around $\mathscr{C}^5$. (b) P^5_- and P^5_+ are plotted together with one branch of $W^s(P^5_-)$ (blue). After approaching P^5_- (in reversed time), $W^s(P^5_-)$ escapes to infinity. A neighborhood of P^5_- is magnified in the box, where a portion of $W^u(P^5_+)$ is included (red). Parameters are fixed at $(\mu, \delta/(2\pi)) = (1, 0.0097)$.

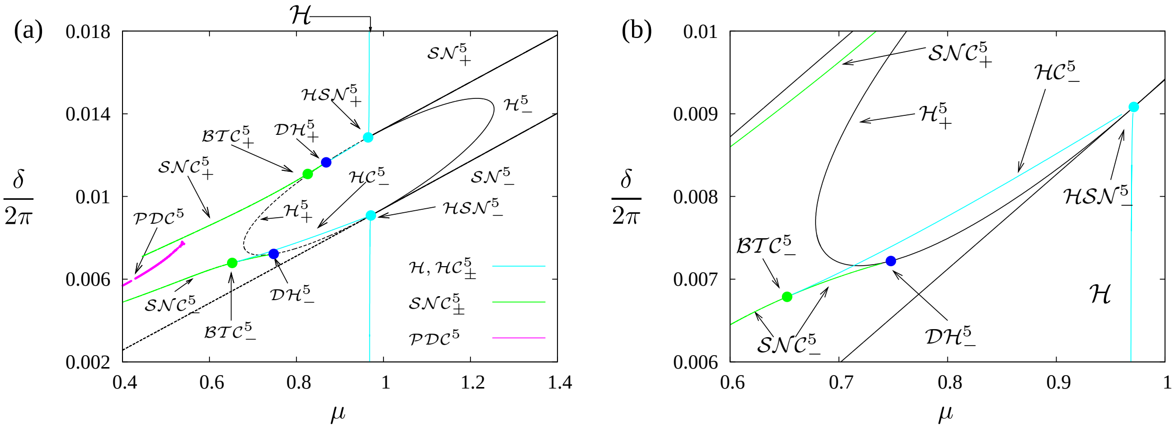

Fig. 11. (a) Bifurcation diagram of G near the 1:5 "bubble", see the text for the notation. The left half of curve $\mathcal{SN}^5_+$ is omitted for better visualization, compare with Fig. 7 left. (b) Magnification of (a). The curves $\mathcal{SNC}^5_\pm$, $\mathcal{HC}^5_\pm$, $\mathcal{PDC}^5_\pm$ and $\mathcal{H}$ are not (expected to be) smooth submanifolds of $\mathbb{R}^2$, but frayed bifurcation boundaries, see Section 2.

resonance "bubbles" with their complex subordinate bifurcation structures is the main reason why the numerical continuation of quasi-periodic bifurcations is difficult.

4.2. Quasi-periodic Saddle-node Bifurcations

A partial bifurcation diagram for the map G is shown in Fig. 11. The curves $\mathcal{SN}^5_\pm$ and $\mathcal{H}^5_\pm$ are saddle-node and Hopf bifurcations of period five points: $\mathcal{SN}^5_\pm$ are the same as in Fig. 7 left and $\mathcal{H}^5_\pm$ are the Hopf bifurcations where the period five invariant circle $\mathscr{C}^5$ of Fig. 10 branches off from the period five point P^5_-, also compare with Fig. 8 right. The frayed quasi-periodic Hopf boundary $\mathcal{H}$ was discussed in the previous section and we refer to [21] for the codimension two points $\mathcal{DH}^5_\pm$, $\mathcal{BTC}^5_\pm$ and $\mathcal{HSN}^5_\pm$.

In this section, we focus on quasi-periodic saddle-node bifurcations of the period five invariant circle $\mathscr{C}^5$. Such bifurcations occur on the two frayed bifurcation boundaries $\mathcal{SNC}^5_\pm$ of Fig. 11. As

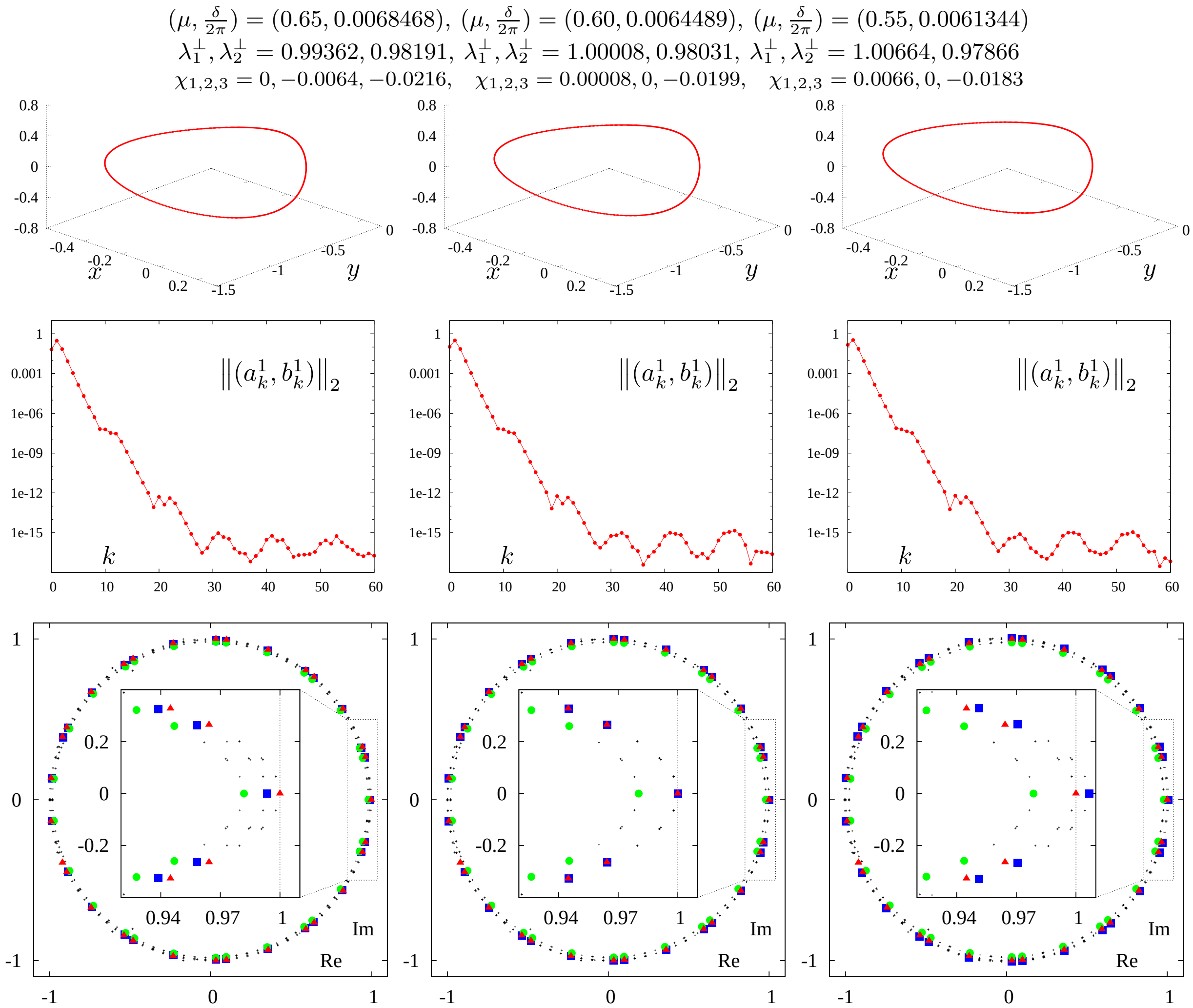

Fig. 12. Quasi-periodic saddle-node bifurcation of an invariant circle of the map G^5 (4.1) (see text for details). Top row: invariant circle for three values of $(\mu, \delta/2\pi)$ (indicated on top of each panel), with rotation number fixed to $\rho = 0.095734978819136$. Left: attracting circle. center, right: unstable circle (saddle type). In all 3 cases the normal eigenvalues $\lambda_{1,2}^\perp$ are real: their values and related Lyapunov exponents $\chi_1 \geqslant \chi_2 \geqslant \chi_3$ are shown on top of each panel. Middle row: modulus $\left\|(a_k^1, b_k^1)\right\|_2$ of the Fourier coefficients of the x-component of the parametrization of the invariant circle on top as a function of k. Bottom row: eigenvalues of the discretized transfer operator (3.11) in $\mathbb{C}$. Magnifications in the insets illustrate the existence of three classes of related eigenvalues of (3.11), corresponding to three separate circles in $\mathbb{C}$. Eigenvalues which our algorithm identifies as sufficiently precise are plotted with either thick dots (green), triangles (red), or squares (blue) according to which class they are assigned to. The remaining ones are plotted in black. The triangles (red) denote the class of the unit eigenvalue in the tangent direction. The blue squares (green dots) correspond to the eigenvalue $\lambda_1^\perp$ ($\lambda_2^\perp$) which is (is not) involved in the bifurcation process.

usual, we start by fixing a (Diophantine) rotation number and describing the bifurcation process as parameters (μ, δ) are "slided" along a single quasi-periodic "hair". We find it convenient to use the fifth image G^5 for both the illustrations and the numerical computations. This allows us to consider any of the five circles of $\mathscr{C}^5$, which are invariant under G^5: in the sequel, we fix one of them and call it *invariant circle* by abuse of notation.

Fig. 12 top shows the invariant circle $\mathscr{C}^5$ for three values of (μ, δ), corresponding to an attractor, a weakly unstable circle (very close to the quasi-periodic saddle-node bifurcation) and an unstable circle. The invariant circle is analytic in all cases, as indicated by the fast decay of the modulus of the Fourier coefficients as a function of the wavenumber k. In this case we used $N = 60$ for the order

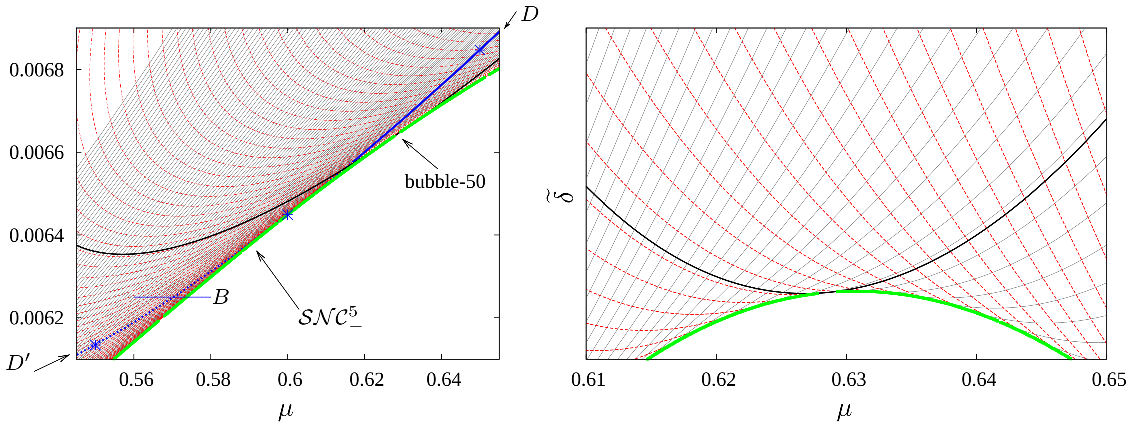

Fig. 13. Left: Cantor-like foliation of curves in the (μ, δ) parameter plane where the invariant circle of Fig. 12 has a fixed irrational rotation number ρ and is stable (grey, solid) or unstable (red, dashed). Green dots: quasi-periodic saddle-node bifurcations on frayed boundary $\mathcal{SNC}^5_-$, where the "hairs" of the Cantor-like foliation are *folded*, see text for details. Black: resonance gap of order 50 on the invariant circle. Asterisks mark the three pairs of parameter values of Fig. 12 (left, middle, right column), belonging to quasi-periodic "hair" defined by $\rho = 0.095734978819136$ constant on the invariant circle $\mathscr{C}^5_\pm$. This "hair" is formed by the union $D \cup D'$ (blue), with $\mathscr{C}^5_-$ stable on D and $\mathscr{C}^5_-$ unstable on D'. See Fig. 14 for the meaning of line B. Right: magnification of left near a 3D Chenciner "bubble", at the "tangency" of frayed boundary $\mathcal{SNC}^5_-$ with the resonance gap of order 50 (black) on the invariant circle $\mathscr{C}^5_\pm$. The plot is deformed for better visibility, using a transformed variable $\widetilde{\delta} = \delta - A * \mu - B$ on the vertical axis. The difference in rotation number between any two consecutive curves is about 0.0003 for both the right and left panel.

of the Fourier truncation in (3.5). A smaller value of 30 or 40 would have sufficed, as suggested by the middle row of Fig. 12.

The bottom row of Fig. 12 illustrates the normal behavior of the invariant circles in the top row. As for Fig. 6, our algorithm indicates reducibility of the linearized dynamics on the circle, since the eigenvalues of the discretized transfer operator (3.11) all lie on circles in the complex plane. In all cases, we identify three distinct circles of eigenvalues and hence three distinct values of $(\lambda^{\parallel}, \lambda^{\perp}_1, \lambda^{\perp}_2)$. We observe numerically that:

$\lambda^{\parallel} = 1$: corresponding to the tangent direction along the invariant circle;

$\lambda^{\perp}_1 > \lambda^{\perp}_2$: the two normal eigenvalues are real and distinct, corresponding to dynamics of node type in the normal direction.

For the center and right columns of Fig. 12, instability of the invariant circle is identified by one circle of eigenvalues outside the unit circle: this corresponds to a positive maximal Lyapunov exponents χ_1.

The three invariant circles of Fig. 12 occur for parameter values belonging to one and the same Diophantine "hair" in the (μ, δ)-plane. This is illustrated in Fig. 13, showing the organisation of the Cantor-like foliation of "hairs" for this quasi-periodic saddle-node bifurcation. Each "hair" is divided by the bifurcation point in two parts D and D', corresponding to stable and unstable normal linear dynamics. The union $D \cup D'$ forms a smooth curve, as opposed to Fig. 2. As a matter of fact, $D_j \cup D'_j$ in Fig. 2 actually form smooth curves in a higher dimensional space, for instance in the (λ, μ, z)-space. The occurrence of cusps at Q_j in Fig. 2 is due to the projection. This is usual for saddle-node bifurcations, compare with the "standard" cusp $y^2 = x^3$.

The frayed bifurcation boundary $\mathcal{SNC}^5_-$ is the *envelope* of the Cantor-like foliation at the bifurcation points. Hence, the projection of the Cantor-like foliation onto the (μ, δ)-parameter plane has a **fold**. A stable and a saddle-like invariant circle coexist in phase space for the same (given) pair of (μ, δ) values, but the two circles have *different* rotation numbers. Suppose to move the parameters (μ, δ) along a straight line towards the bifurcation boundary $\mathcal{SNC}^5_-$. Then the two

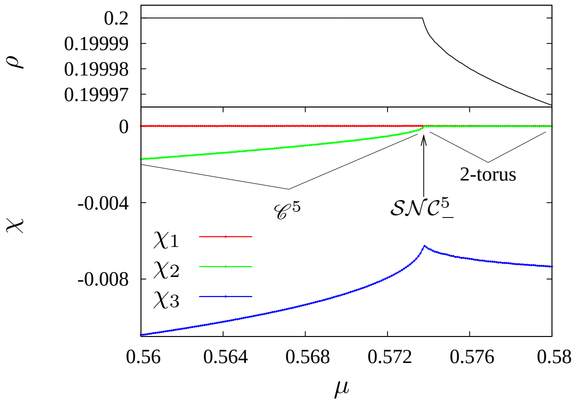

Fig. 14. Lyapunov exponents $\chi_1 \geqslant \chi_2 \geqslant \chi_3$ (bottom part of the panel) and rotation number ρ around the origin (top part) as a function of μ varying along the horizontal line B in Fig. 13 left, for fixed $\delta/2\pi = 0.00625$.

invariant circles undergo different resonances at different parameter values. The straight line might cross $\mathcal{SNC}^5_-$ inside a resonance "bubble", with the ensuing complicated dynamics described by Chenciner [30–32].

On the other hand, the quasi-periodic saddle-node bifurcation admits a simple dynamical description when parameters are constrained to vary on a single Diophantine "hair", as Fig. 12 shows. Along this "hair", a stable and an unstable invariant circle, both of node type and with *the same rotation number*, can be thought of as merging at the bifurcation point coming from the *different directions* of D and D'. In other words, the bifurcating invariant circles with the same (Diophantine) rotation rumber do not coexist at the same parameter values. This description necessitates from at least two parameter values and is somewhat different from the standard saddle-node bifurcation for fixed points. However, *it is the most natural* for quasi-periodic saddle-node bifurcations.

Fig. 14 shows the variation of the three Lyapunov exponents as the parameter μ varies along line labelled B in Fig. 13 left. For large μ, say $\mu = 0.58$, the dynamics takes place on the 2-torus attractor, as indicated by two vanishing Lyapunov exponents. This corresponds to the green domain in the Lyapunov diagram of Fig. 7 right. At the left of Fig. 14, say for $\mu = 0.56$, the dynamics takes place on the period five circle attractor $\mathscr{C}^5$ of Fig. 12 left. When μ increases across the value 0.574 (marked by an arrow in Fig. 14), the second Lyapunov exponent vanishes (with a square-root asymptotics): this is where the quasi-periodic saddle-node bifurcation takes place. Note that the 2-torus reappears immediately after. Indeed, this bifurcation *takes place on the invariant 2-torus.*

This is illustrated in Fig. 15. The period 5 circle attractor $\mathscr{C}^5$ coexists in phase space with a period 5 saddle-like circle. To distinguish them, we denote the attractor by $\mathscr{C}^5_-$ and the saddle by $\mathscr{C}^5_+$. In fact, they are part of the same (folded) family of invariant circles but their rotation numbers are different, as discussed above. The unstable manifold $W^u(\mathscr{C}^5_+)$ is attracted by $\mathscr{C}^5_-$ and the union $W^u(\mathscr{C}^5_+) \cup \mathscr{C}^5_-$ forms a *phase-locked* 2-torus, which is only finitely differentiable. In this sense, one may say that the center manifold of this quasi-periodic saddle-node bifurcation is the 2-torus itself. For the choice of parameter values of Fig. 15, the phase-locked 2-torus is **not** normally hyperbolic, since the normal instability at the saddle $\mathscr{C}^5_+$, given by $\chi_1 = 0.0216$ (corresponding to λ^+_1) is larger than the normal compression at the node $\mathscr{C}^5_-$, given by $\chi_3 = -0.0122$.

Chenciner-like "bubbles" are visible along $\mathcal{SNC}^5_-$ (as opposed to $\mathcal{H}$, see Section 4.1). A resonance "bubble" of order 50 is pointed to by an arrow in Fig. 13 left and magnified in the right panel. The black line actually consists of a pair of very narrowly spaced saddle-node bifurcation curves of period 50 points. These two curves delimit a narrow resonance gap where the attracting invariant circle $\mathscr{C}^5_-$ is phase-locked to a period 50 attracting orbit.

The resonance gap is laid out in the parameter plane in a similar fashion as to the quasi-periodic "hairs" and has a quadratic "tangency" with the frayed boundary $\mathcal{SNC}^5_-$ at a Chenciner-like

	ρ	$\lambda^{\parallel}$	$\lambda_1^{\perp}$	$\lambda_2^{\perp}$
$\mathscr{C}_+^5$	0.11109156678918	1.0	1.02186825875584	0.99929673737074
$\mathscr{C}_-^5$	0.08812166712298	1.0	0.98788853248803	0.95388810564241

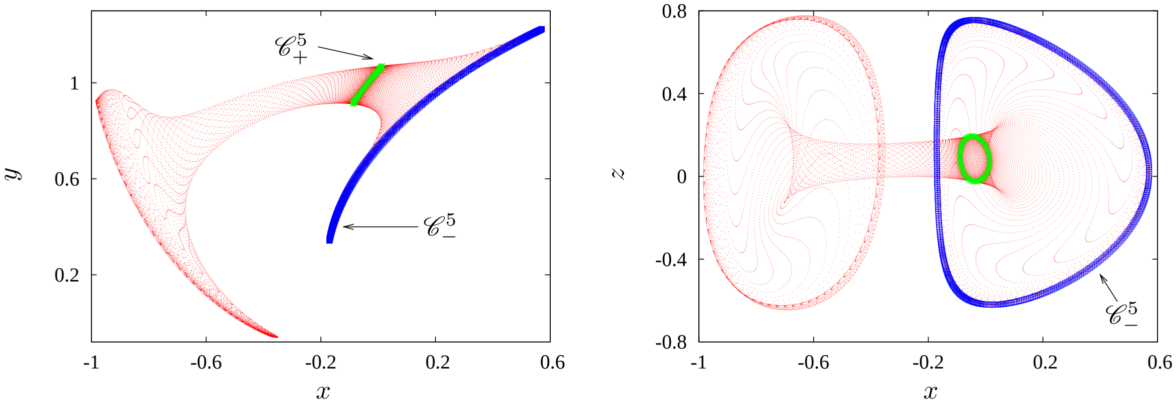

Fig. 15. Projection on (x, y) (left) and on (x, z) (right) of the saddle-like period five invariant circle $\mathscr{C}_+^5$ (green) with both sides of $W^u(\mathscr{C}_+^5)$ (red) and with the period five circle attractor $\mathscr{C}_-^5$ (blue), for $(\mu, \delta/(2\pi)) = (0.746752823430779, 0.009760780820012)$, rotation numbers and eigenvalues are given on top. The fifth iterate G^5 of map (4.1) is used for the numerical computations, hence only one "fifth" of the whole 2-torus of G is shown.

"bubble" where $\mathcal{SNC}_-^5$ is interrupted. One expects a dense set of such "bubbles" along $\mathcal{SNC}_-^5$: most bubbles are "tiny" and go undetected by our algorithm. A few larger "bubbles" occur such as that of Fig. 13 right: they are "skipped" by our algorithm thanks to the restriction to Diophantine rotation numbers described in Section 3.2. At each "bubble" one expects all the complexity described in [30–32] and even more, since we are in a 3D case as opposed to the planar case considered there.

4.3. Quasi-periodic Period Doubling Bifurcations

Fig. 16 illustrates a quasi-periodic period doubling bifurcation of the invariant circle $\mathscr{C}^5$. Once again, we use the fifth iterate G^5. Although it would be more natural to consider a fixed rotation number as we did above, the invariant circle $\mathscr{C}^5$ this time has *different* rotation numbers in the three cases of Fig. 16, whereas we keep fixed the parameter δ. The reason for our choice will become clear below.

The invariant circle $\mathscr{C}^5$ is attracting in Fig. 16 left, weakly unstable and unstable in Fig. 16 center and right, respectively. A "doubled" circle $2\mathscr{C}^5$ coexists with $\mathscr{C}^5$ in Fig. 16 right. This bifurcation is of **length-doubling** type, in the sense that $2\mathscr{C}^5$ is a single connected curve of roughly twice the length (and half the rotation number) of $\mathscr{C}^5$, see [33, 51, 52]. In this case, the center manifold of the bifurcation is a Möbius strip. Section 5 describes quasi-periodic period doublings which give rise to a pair of disjoint curves, each mapped onto each other by the iterates of the map. In that case, the center manifold is a cylinder.

The invariant circle $\mathscr{C}^5$ is analytic in all cases, but the decay of the Fourier coefficients in Fig. 16 (middle row) is here much slower than above (middle rows of Fig. 6 and 12). We herefore used $N = 180$ for the order of the Fourier truncation (3.5). The numerically computed spectrum of the discretized transfer operator indicates reducibility of the normal linear dynamics for $\mathscr{C}^5$. In all panels of Fig. 16 (bottom row), we identify three distinct circles of eigenvalues, corresponding to distinct values of $(\lambda^{\parallel}, \lambda_1^{\perp}, \lambda_2^{\perp})$. Once again we find $\lambda^{\parallel} = 1$, corresponding to the tangent direction along the invariant circle $\mathscr{C}^5$. However, the eigenvalues $\lambda_{1,2}^{\perp}$ produced by the method of Section 3.1 are *complex* and **not conjugate**. This is due to the non-orientability of the corresponding linear bundles (eigendirections). Hence we use the *double covering trick* described in [42–44]. This shows that the two complex eigenvalues $\lambda_{1,2}^{\perp}$ actually correspond to the real and distinct eigenvalues

$$\rho = 0.953971309286931, \quad \rho = 0.954156809441970, \quad \rho = 0.954434915451831$$
$$(\mu, \tfrac{\delta}{2\pi}) = (0.3415, 0.00506),\ (\mu, \tfrac{\delta}{2\pi}) = (0.3409, 0.00506),\ (\mu, \tfrac{\delta}{2\pi}) = (0.34, 0.00506)$$
$$\widetilde{\lambda_1^\perp}, \widetilde{\lambda_2^\perp} = 0.9967, 0.8717,\ \widetilde{\lambda_1^\perp}\widetilde{\lambda_2^\perp} = 1.00002, 0.8685,\ \widetilde{\lambda_1^\perp}, \widetilde{\lambda_2^\perp} = 1.0047, 0.8639$$
$$\chi_{1,2,3} = 0, -0.00327, -0.1372,\ \chi_{1,2,3} = 0.0002, 0, -0.1410,\ \chi_{1,2,3} = 0.00467, 0, -0.1463$$

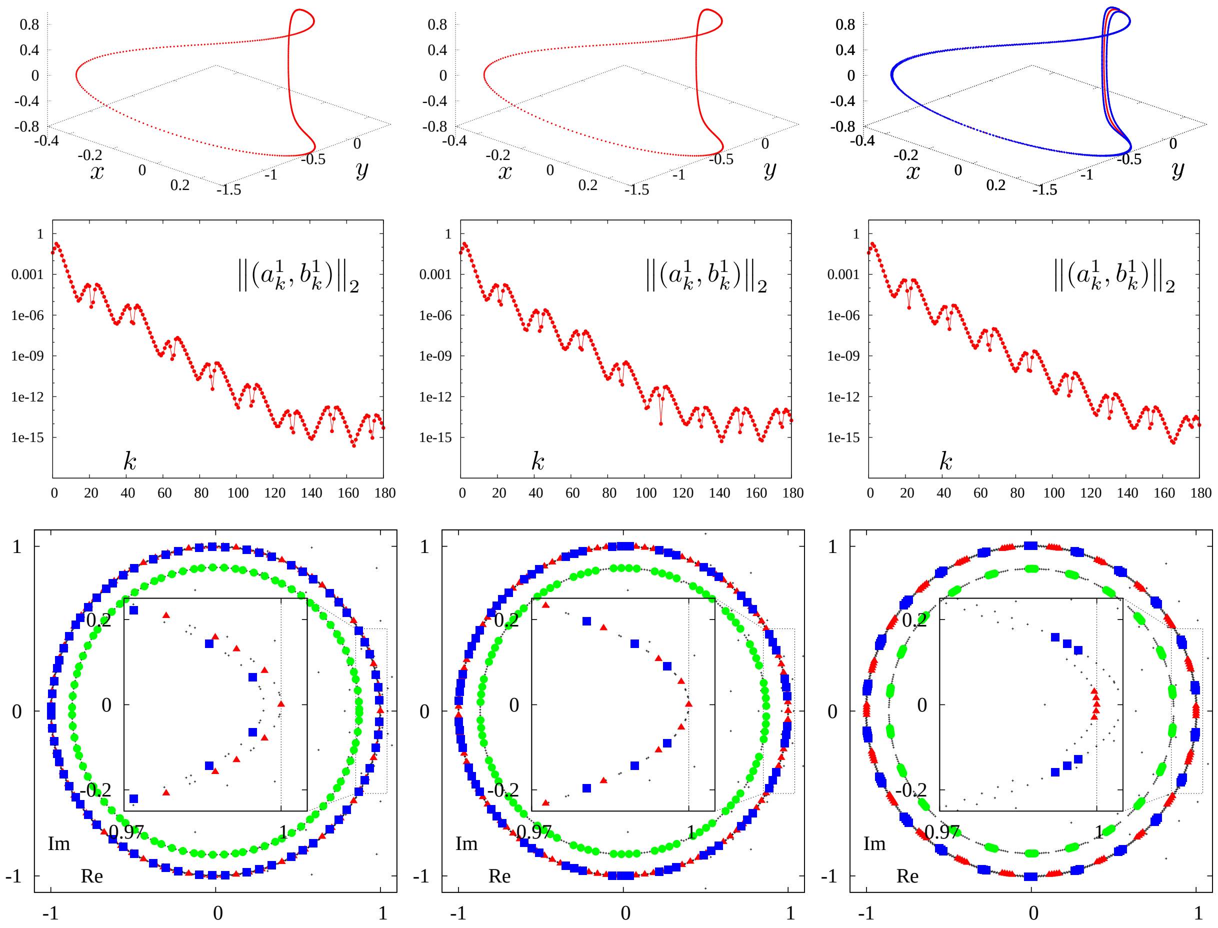

Fig. 16. Quasi-periodic period-doubling bifurcation of period 5 invariant circle $\mathscr{C}^5$ of (4.1). Top row: $\mathscr{C}^5$ for three values of μ (shown on top of each panel, with the three different ρ) and $\delta/2\pi = 0.00506$ fixed. Left: attracting circle. center: weakly unstable $\mathscr{C}^5$ (saddle type). Right: unstable $\mathscr{C}^5$ (red) which coexists with an attracting doubled circle $2\mathscr{C}^5$ (blue). In all cases the normal eigenvalues of (3.11) are in $\mathbb{C}$, but correspond to $\widetilde{\lambda_{1,2}^\perp} \in \mathbb{R}$ using the "double covering trick", see text. The related Lyapunov exponents $\chi_1 \geqslant \chi_2 \geqslant \chi_3$ are shown on top of each panel. Middle row: modulus $\left\|(a_k^1, b_k^1)\right\|_2$ of the Fourier coefficients of the x-component of the parametrization of the circle on top as a function of k. Bottom row: eigenvalues of (3.11) in $\mathbb{C}$. Magnifications in the insets illustrate the existence of three classes of related eigenvalues of (3.11), corresponding to three separate circles in $\mathbb{C}$. Eigenvalues which our algorithm identifies as sufficiently precise are plotted with either thick dots (green), triangles (red), or squares (blue) according to which class they are assigned to. The remaining ones are plotted in black. The triangles (red) denote the class of the unit eigenvalue in the tangent direction. The green dots (blue squares) correspond to the eigenvalue $\widetilde{\lambda_1^\perp}$ ($\widetilde{\lambda_2^\perp}$) which is (is not) involved in the bifurcation process.

$\widetilde{\lambda_{1,2}^\perp}$ indicated on top of Fig. 16, indicating dynamics of node type in the normal direction, as we expected.

Fig. 17 shows the organization of the quasi-periodic "hairs" for this bifurcation scenario. The frayed boundary of quasi-periodic doublings, identified by the thick dots, is nearly aligned with the "hairs" of the Cantor-like foliation. This makes it difficult to visualise the crossing of the unit circle illustrated in the middle row of Fig. 16, if parameters are moved along a single "hair". For this reason we chose to keep δ fixed in Fig. 16, instead of fixing the rotation number. Also for this

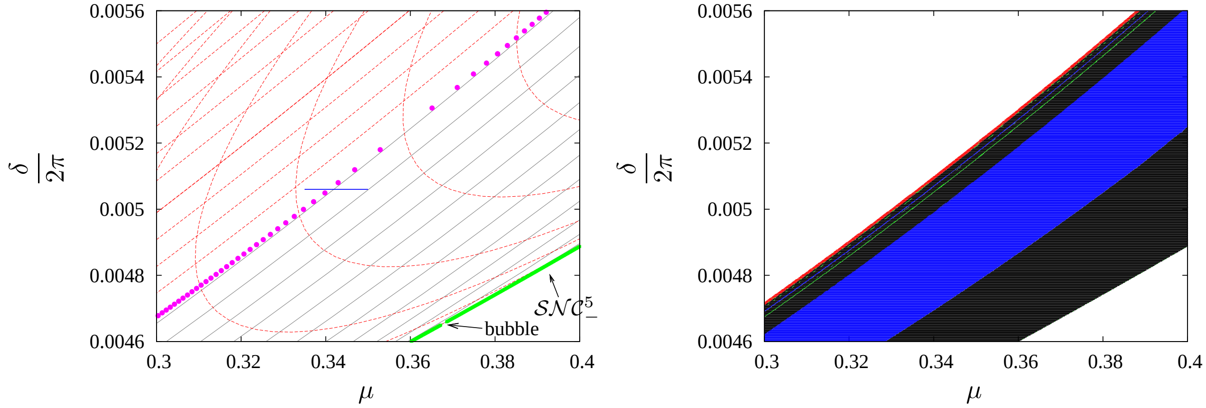

Fig. 17. Left: Cantor-like foliation of curves in the (μ, δ) parameter plane where the invariant circle of Fig. 16 has a fixed irrational rotation number ρ and is stable (grey, solid) or unstable (red, dashed). The difference in rotation number between any two consecutive curves is 0.002565. Magenta dots: quasi-periodic period doubling bifurcations belonging to frayed boundary $\mathcal{PDC}^5$. Green dots: quasi-periodic saddle-node bifurcations on frayed boundary $\mathcal{SNC}_-^5$. The three pairs of parameter values of Fig. 16 belong to the horizontal segment (blue) crossing the frayed boundary $\mathcal{PDC}^5$. Lyapunov exponents along this segment are shown in Fig. 18. Right: Lyapunov diagram of attractor for the same parameter window as Left, see Tab. 2 for the color coding.

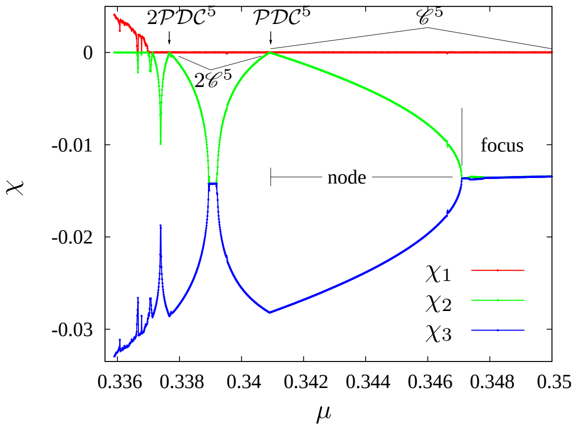

Fig. 18. Lyapunov exponents $\chi_1 \geqslant \chi_2 \geqslant \chi_3$ as a function of μ varying along the small horizontal segment in Fig. 17 left, corresponding to fixed $\delta/2\pi = 0.00506$.

reason, to locate these doubling bifurcations we had to compute many "hairs" for rotation number varying in a relatively narrow interval of values.

Fig. 18 shows the variation of the Lyapunov exponents along a line of constant δ (shown as a small horizontal segment in Fig. 17) across the quasi-periodic doubling boundary. Quasi-periodic dynamics seems to be abundant in the sense of measure, since the maximal Lyapunov exponent χ_1 never becomes significantly negative, as it would be if the invariant circle is phase-locked to a periodic attractor. The rightmost vanishing of χ_2 near $\mu = 0.341$ occurs at the quasi-periodic doubling boundary $\mathcal{PDC}^5$, see Fig. 11 left. Across this bifurcation, for μ slightly smaller than 0.341, the doubled circle attractor $2\mathscr{C}^5$ is detected. Note that both circles $\mathscr{C}^5$ and $2\mathscr{C}^5$ are of node type near the doubling, that is $\widetilde{\lambda_1^\perp} > \widetilde{\lambda_1^\perp}$ as indicated by the Lyapunov exponents $\chi_2 \neq \chi_3$.

The eigenvalues $\widetilde{\lambda_{1,2}^\perp}$ then become complex conjugate in the narrow interval where $\chi_2 = \chi_3$. This corresponds to normal linear dynamics of focus type. This can be interpreted as the eigenvalues $\widetilde{\lambda_{1,2}^\perp}$ "racing around the origin" inside the complex plane and then re-entering the real axis on the negative side (see e.g. [18, Fig. 12]), as indicated by χ_2 and χ_3 becoming distinct again. This process allows for the eigenvalue $\widetilde{\lambda_1}$ to cross the value -1 again, yielding a second quasi-periodic doubling bifurcation where $2\mathscr{C}^5$ loses stability and a quadrupled circle attractor $4\mathscr{C}^5$ branches off.

As observed in [66–68], unlike the infinite Feigenbaum cascade of period doublings for periodic points, the quasi-periodic doubling process only seems to involve a **finite number** of doublings, after which the invariant circle breaks down and a chaotic attractor appears. For model map G considered here, the ubiquitous presence of resonances on the invariant circles complicates the description. For this reason, we resort to a quasi-periodically driven map in Section 5 to further discuss this phenomenon.

5. EXAMPLE 2: THE QUASI-PERIODICALLY DRIVEN HÉNON DISSIPATIVE MAP

Consider a *quasi-periodically driven Hénon map*:

$$H_{a,b,\gamma}\begin{pmatrix} x \\ y \\ \theta \end{pmatrix} = \begin{pmatrix} 1-(a+\varepsilon\cos(\theta))x^2+y \\ bx \\ \theta+2\pi\gamma \pmod{2\pi} \end{pmatrix}, \tag{5.1}$$

where $\gamma = (\sqrt{5}-1)/2$ is the golden mean. For $\varepsilon = 0$ this reduces to the well-known Hénon dissipative map.

The first problem we consider is: what is the effect of quasi-periodic driving on the period doubling cascade occurring in the Hénon map? Is it possible to detect *lack of reducibility* for some of the invariant circles undergoing the doublings?

To investigate this question, we fix the parameter $b = 0.4$ and look first at the unperturbed case $\varepsilon = 0$ for increasing values of a, see figure 19. We recall that the sum of the two Lyapunov exponents is equal to $\log(b) \approx -0.916291$ for the Hénon map. When the underlying attractor consists of stable periodic points which are of focus type, the two Lyapunov coincide, hence they are both equal to $\log(b)/2 \approx -0.458145$. This criterion can effectively be used to verify (lack of) reducibility.

When the parameter a is increased across the period doubling cascade, the width of the parameter intervals where periodic attractors are of focus type quickly decreases with the period of the attractor, see the top row of 19. Hence, the decrease of the maximal Lyapunov exponent χ to $\log(b)/2 \approx -0.458145$ might go undetected if the a-parameter line is scanned with too coarse steps. The bottom row of Fig. 19 uses the transformed variable $-\log_{10}(a_\infty - a)$ on the horizontal axis: this allows to visualize the geometric scaling between the doublings associated to Feigenbaum's universality.

Let L_k denote the distance between the values a_k and a_{k+1} where the k-th and $(k+1)$-th period doublings occur along the cascade. Then $L_k \approx L_{k-1}/G$, where $G \approx 4.67$ denotes the Feigenbaum constant. It is also easy to check that if F_k denotes the width of the a-parameter intervals for which a stable focus is found between a_k and a_{k+1}, then $F_k \approx CG^kF_{k-1}^2$, where $C \approx G^{-3}$ in the present case. Hence the amplitude of such "stable focus intervals" decreases quadratically instead of linearly.

For a fixed value of k and $\varepsilon > 0$ sufficiently small, map (5.1) has an attracting periodically invariant circle of period 2^k. In other words, there are 2^k disjoint copies of a circle which are mapped one onto another by (5.1). The linearized dynamics around the invariant circles is described by a quasi-periodic skew product whose matrix is

$$\begin{pmatrix} -2(a+\varepsilon\cos(\theta))x(\theta) & 1 \\ b & 0 \end{pmatrix}, \tag{5.2}$$

where $x(\theta)$ is the first component of the orbit on the 2^k invariant circles and the variable θ evolves quasi-periodically according to

$$\theta \to \theta + 2\pi\gamma \pmod{2\pi}.$$

For any $\varepsilon > 0$, the behavior of the maximal Lyapunov exponent χ as a function of a is different than $\varepsilon = 0$ and the differences become more evident for larger ε, see figure 20. The most remarkable difference is that only a *finite number of period doublings* is observed for $\varepsilon > 0$. This period doubling interruption was already observed in [20, 68] for entirely different systems (namely, systems without the skew-product structure of (5.1)).

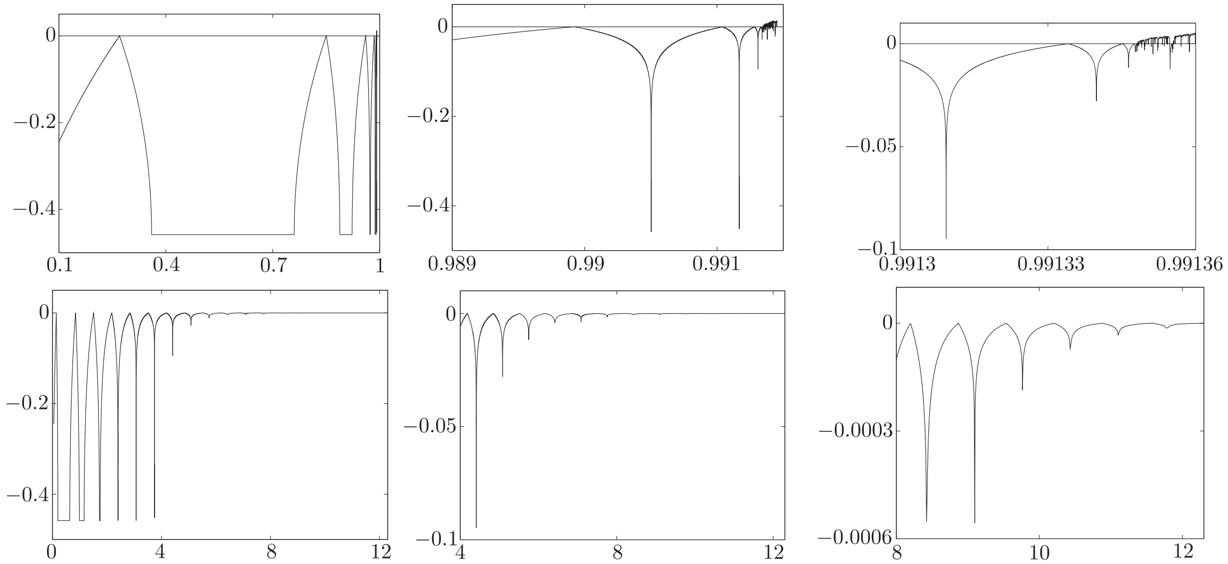

Fig. 19. Illustration of period doublings for the uncoupled Hénon map (map (5.1) with $\varepsilon = 0$) for $b = 0.4$ and varying a. Top row: the maximal Lyapunov exponent χ is represented as a function of a. Note the scaling of the a_k-values where the k-th period doubling occurs and of the width of the intervals with periodic attractors of focus type (see text). The limit of a_k is $a_\infty \approx 0.991348146972$. Bottom row: χ as a function of the transformed variable $-\log_{10}(a_\infty - a)$, in different windows. Up to 19 period doublings can be seen.

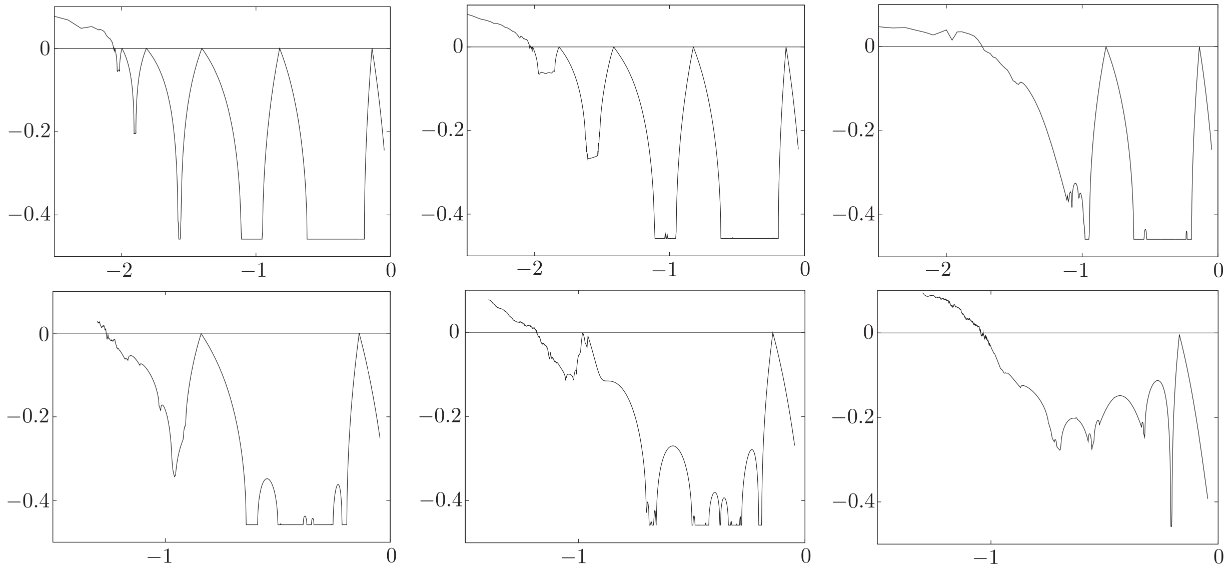

Fig. 20. Illustration of quasi-periodic period doublings for map (5.1) with $\varepsilon > 0$. Plots of χ as a function of $\log_{10}(1 - a)$ for different values of ε: $0.0001, 0.001, 0.01$ for the top row and $0.05, 0.10, 0.25$ for the bottom row, from left to right.

The observed behavior suggests to examine the evolution of the maximal Lyapunov exponent χ and of the rotation number ρ of the skew product (5.2) for small values of ε (e.g. $\varepsilon = 0.0001$), in a

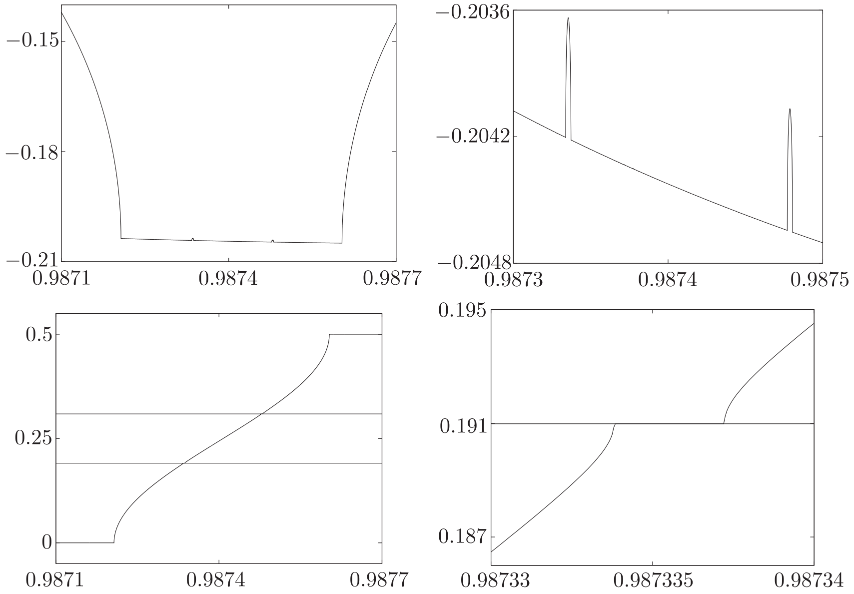

Fig. 21. Illustration of *non-reducibility* through plots of the maximal Lyapunov exponent (top) and of the rotation number (bottom) in a selected domain. Left, bottom: horizontal lines at $\rho = (1-\gamma)/2 \approx 0.190983$ and $\gamma/2 \approx 0.309017$. Right: Magnifications of the left panels, showing 2 bumps in χ (top) and a neighborhood of the leftmost resonance in the rotation number ρ (bottom).

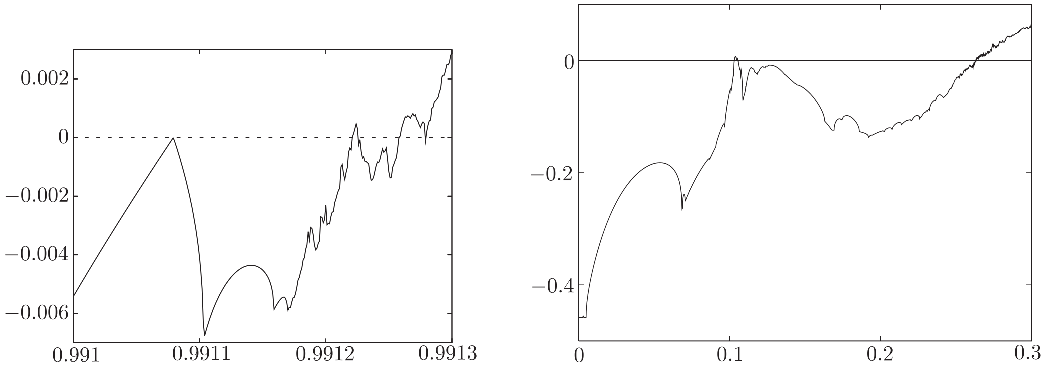

Fig. 22. Left: the "tail" of the period doubling cascade for $\varepsilon = 0.0001$, illustrated by plotting the maximal Lyapunov exponent χ as a function of a. The sixth period-doubling is first seen. For slightly larger a, we would expect a domain characterized by attracting periodically invariant circles of period 2^6 and of focus type. While 2^6 periodic attracting circles still occur, the dynamics is not reducible. Reducibility is recovered in a narrow parameter range and then lost again for larger a. This gives rise to attractors which are either strange non-chaotic or highly folded circles and, finally, chaotic attractors when $\chi > 0$. Right: evolution of χ as a function of ε for fixed $b = 0.4$ and $b = 0.9$. Many phenomena occur which are yet to be clarified.

range of a-parameter values where one suspects that the system is not reducible. We consider values of a larger than the value a_4 of the fourth period doubling. Fig. 21 shows the decrease of χ after the fourth period doubling bifurcation. The value of χ remains far from the value $\log(b)/2$ and, hence, the two Lyapunov exponents *remain different*. At the same time the rotation number is changing. This is not compatible with the reduction to constant coefficients of the normal linear dynamics. In this parameter range the maximal Lyapunov exponent χ displays two tiny "bumps" as a is varied, see the magnification in the top right panel. The bottom right panel of Fig. 21 shows a detail of the rotation number when it crosses the value $(1-\gamma)/2$, corresponding to a resonance. The methods used for the computations of Fig. 21 and the relation to (lack of) reducibility are discussed in [56, 57], where applications are presented to skew-products in the discrete and continuous case.

Fig. 22 presents additional phenomena near the *interruption of the cascade* in the present case. For $\varepsilon = 0.0001$ the fourth, fifth and sixth quasi-periodic period doublings occur at the values $a_4 \approx 0.98469395$, $a_5 \approx 0.98992364$ and $a_6 \approx 0.99107925$, respectively. The ratio $(a_5 - a_4)/(a_6 - a_5) \approx 4.53$ is still not too far from Feigenbaum's value. Based on that ratio we could extrapolate the location of a_7 at 0.99133435 (this "prediction" works well in the autonomous case $\varepsilon = 0$). However, strange attractors are already found before the "predicted" value of a_7. Fig. 22 left shows the evolution of χ starting from a slightly smaller than a_6 until the entrance in the chaotic range. Until $a \approx 0.991182$ a clear-cut domain is first found, where the attractor consists of 2^6 circles. Then, until $a \approx 0.991257$ the attractor seems to consist of highly folded 2^6 circles, or to be a *strange non-chaotic attractor*, except for a tiny domain nearby $a = 0.991223$ where a strange attractor is detected, $\chi > 0$. Finally, from $a \approx 0.991257$ the attractor is definitely strange.

The evidence based on the value of χ was complemented by direct inspection of plots of the attractors. The domain of non-reducibility in Fig. 21 is roughly

$$[0.987207, 0.987603] \subset [a_4, a_5] :$$

this is the first such domain found for increasing a. A second such domain is approximately $[0.990330, 0.990724] \subset [a_5, a_6]$, again located in the range where one would expect invariant circles of stable focus type. In both cases the attractors are still periodically invariant circles of period 2^k, but the dynamics is not of focus type. A third non-reducibility domain starts at $a \approx 0.991104$ and no further domains of reducibility are found for larger a. Note that in this last domain there is a first subdomain where the attractor consists of 2^6 circles beyond becoming a strange non-chaotic or chaotic attractor. Hence, non-reducibility of the linearized quasi-periodic skew product is compatible with the existence of invariant circles.

Finally in figure 22 the maximal Lyapunov exponent is plotted as a function of ε for b fixed at $b = 0.4$, $a = 0.9$. For ε increasing from 0, many phenomena occur which are yet unclear, although it seems that they are not only related to the loss of reducibility.

6. CONCLUSIONS

The theory of quasi-periodic bifurcations presents a number of unsolved challenging problems and a considerable amount of work is needed to further both the theoretical understanding and the numerical algorithms.

On the theoretical side we list three major lines.

1. Can a generic theory be developed for the dynamics of a resonance "bubble"? Examples of particular case studies are [2, 30–32, 61] for a planar quasi-periodic saddle-node bifurcation and [21] for a 3D quasi-periodic Hopf. Not much is known for normal-internal resonances, see [19, 26, 71].

2. It would be useful to develop a quasi-periodic bifurcation theory in the *far from integrable* case (compare Section 2.1), possibly along the lines of [50]. That is, a theory which is directly applicable to models such as those analyzed in this paper, or more general systems found in applications, such as [20, 53, 58, 66, 73].

3. Basically nothing is known about quasi-periodic bifurcations for non-reducible invariant circles, see [40, 41, 44, 49, 56, 57]. For a treatment of the skew Hopf bifurcation see [23, 25, 27, 65, 72].

The numerical algorithm proposed here is largely confined to systems with a few degrees of freedom. The computations quickly become too cumbersome for larger phase space dimension. Recently developed parallel algorithms may remedy this problem [48], although the computation of the normal behavior by the approach of [47] may still remain intractable for larger systems. Appealing alternatives may be the *fractional iteration* method [63, 64] (see Section 3.1) and the *reducibility method* proposed in [42–44]. The latter seems particularly powerful in that it allows to compute the *dynamics on the torus*, as well as an approximation for the torus itself. It would be very interesting to apply this method to systems where the frequency changes with the control parameters, such as those considered here. The lack of reducibility is, of course, a major open problem for all numerical algorithms.

ACKNOWLEDGMENTS

R.V. gratefully acknowledges support by the Willis Research Network[2)] and is indebted to the Universities of Barcelona and Groningen for kind hospitality. C.S. has been supported by grants MTM2006-05849/Consolider (Spain) and CIRIT 2008 SGR-67 (Catalonia).

REFERENCES

1. Arnold, V. I., *Geometrical Method in the Theory of Ordinary Differential Equations,* New York–Berlin: Springer, 1983.
2. Baesens, C., Guckenheimer, J., Kim, S., and MacKay, R. S., Three Coupled Oscillators: Mode-locking, Global Bifurcations and Toroidal Chaos, *Phys. D,* 1991, vol. 49, no. 3, pp. 387–475.
3. Braaksma, B. L. J. and Broer, H. W., On a Quasi-Periodic Hopf Bifurcation, *Ann. Inst. H. Poincaré Anal. Non Linéaire,* 1987, vol. 4, no. 2, pp. 115–168.
4. Braaksma, B. L. J., Broer, H. W., and Huitema, G. B., Towards a Quasi-Periodic Bifurcation Theory, *Mem. Amer. Math. Soc.,* 1990, vol. 83, no. 421, pp. 83–175.
5. Broer, H. W., Formal Normal Forms Theorems for Vector Fields and Some Consequences for Bifurcations in the Volume Preserving Case, *Dynamical Systems and Turbulence, Warwick 1980 (Coventry, 1979/1980),* A. Dold and B. Eckmann (Eds.), Lecture Notes in Math., vol. 898, Berlin–New York: Springer, 1980, pp. 54–74.
6. Broer, H. W., Normal Forms in Perturbation Theory, *Encyclopædia of Complexity & System Science,* R. Meyers (Ed.) New York: Springer, 2009, pp. 6310–6329.
7. Broer, H. W., Ciocci, M. C., and Hanßmann, H., The Quasi-Periodic Reversible Hopf Bifurcation, *Internat. J. Bifur. Chaos Appl. Sci. Engrg.,* 2007, vol. 17, no. 8, pp. 2605–2623.
8. Broer, H. W., Ciocci, M. C., Hanßmann, H., and Vanderbauwhede, A., Quasi-Periodic Stability of Normally Resonant Tori, *Phys. D,* 2009, vol. 238, no. 3, pp. 309–318.
9. Broer, H. W., Hanßmann, H., and Hoo, J., The Quasi-Periodic Hamiltonian Hopf Bifurcation, *Nonlinearity,* 2007, vol. 20, no. 2, pp. 417–460.
10. Broer, H. W., Hanßmann, H., Jorba, À., Villanueva, J., and Wagener, F. O. O., Normal-Internal Resonances in Quasi-Periodically Forced Oscillators: A Conservative Approach, *Nonlinearity,* 2003, vol. 16, no. 5, pp. 1751–1791.
11. Broer, H. W., Hanßmann, H., and You, J., Bifurcations of Normally Parabolic Tori in Hamiltonian Systems, *Nonlinearity,* 2005, vol. 18, no. 4, pp. 1735–1769.
12. Broer, H. W., Hanßmann, H., and You, J., Umbilical Torus Bifurcations in Hamiltonian Systems, *J. Differential Equations,* 2006, vol. 222, no. 1, pp. 233–262.
13. Broer, H. W., Hanßmann, H., and You, J., On the Destruction of Resonant Lagrangean Tori in Hamiltonian Systems, *Preprint, Mathematisch Instituut, Universiteit Utrecht,* Utrecht, 2008.
14. Broer, H. W., Hanßmann, and Wagener, F. O. O., Quasi-Periodic Bifurcation Theory, the Geometry of KAM, *in preparation.*
15. Broer, H. W., Holtman, S. J., Vegter, G., and Vitolo, R., Dynamics and Geometry Near Resonant Bifurcations, *Regul. Chaotic Dyn.,* 2011, vol. 16, nos. 1–2, pp. 40–51.
16. Broer, H. W., Hoo, J., and Naudot, V., Normal Linear Stability of Quasi-Periodic Tori, *J. Differential Equations,* 2007, vol. 232, no. 2, pp. 355–418.
17. Broer, H. W., Huitema, G. B., and Takens, F., Unfoldings of Quasi-Periodic Tori, *Mem. Amer. Math. Soc.,* 1990, vol. 83, no. 421, pp. 1–82.
18. Broer, H. W., Simó, C., Tatjer, J. C., Towards Global Models Near Homoclinic Tangencies of Dissipative Diffeomorphisms, *Nonlinearity,* 1998, vol. 11, no. 3, pp. 667–770.
19. Broer, H. W., van Dijk, R., and Vitolo, R., Survey of Strong Normal-Internal $k : l$ Resonances in Quasi-Periodically Driven Oscillators for $l = 1, 2, 3$, *Proceedings SPT 2007, Internat. Conf. on Symmetry and Perturbation Theory (Otranto (Italy), 2–9 June 2007),* G. Gaeta, R. Vitolo, S. Walcher (Eds.), Hackensack, NJ: World Sci. Publ., 2008, pp. 45–55.
20. Broer, H. W., Simó, C., and Vitolo, R., Bifurcations and Strange Attractors in the Lorenz-84 Climate Model with Seasonal Forcing, *Nonlinearity,* 2002, vol. 15, no. 4, pp. 1205–1267.
21. Broer, H. W., Simó, C., and Vitolo, R., The Hopf-Saddle-Node Bifurcation for Fixed Points of 3*D*-diffeomorphisms: Analysis of a resonance "bubble", *Phys. D,* 2008, vol. 237, no. 13, pp. 1773–1799.
22. Broer, H. W., Simó, C., and Vitolo, R., The Hopf-Saddle-Node Bifurcation for Fixed Points of 3*D*-diffeomorphisms: The Arnol′d Resonance Web, *Bull. Belg. Math. Soc. Simon Stevin,* 2008, vol. 15, no. 5, pp. 769–787.
23. Broer, H. W. and Takens, F., Mixed Spectrum and Rotational Symmetry, *Arch. Ration. Mech. Anal.,* 1993, vol. 124, pp. 13–42.

[2)] www.willisresearchnetwork.com

24. Broer, H. W. and Takens, F., *Dynamical Systems and Chaos*, Appl. Math. Sci., vol. 172, New York: Springer, 2011.
25. Broer, H. W., Takens, F., and Wagener, F. O. O., Integrable and Non-Integrable Deformations of the Skew Hopf Bifurcation, *Regul. Chaotic Dyn.,* 1999, vol. 4, no. 2, pp. 16–43.
26. Broer, H. W. and Vegter, G., Generic Hopf–Neĭmark–Sacker Bifurcations in Feed Forward Systems, *Nonlinearity,* 2008, vol. 21, pp. 1547–1578.
27. Broer, H. W. and Wagener, F. O. O., Quasi-Periodic Stability of Subfamilies of an Unfolded Skew Hopf Bifurcation, *Arch. Ration. Mech. Anal.,* 2000, vol. 152, pp. 283–326.
28. Castellà, E., Sobre la dinàmica prop dels punts de Lagrange del sistema Terra–Luna, *PhD thesis,* Univ. of Barcelona, 2003.
29. Castellà, E. and Jorba, À., On the Vertical Families of Two-Dimensional Tori Near the Triangular Points of the Bicircular Problem, *Celestial Mech. Dynam. Astronom.,* 2000, vol. 76, no. 1, pp. 35–54.
30. Chenciner, A., Bifurcations de points fixes elliptiques: I. Courbes invariantes, *Inst. Hautes Études Sci. Publ. Math.,* 1985, vol. 61, pp. 67–127.
31. Chenciner, A., Bifurcations de points fixes elliptiques: II. Orbites périodiques et ensembles de Cantor invariants, *Invent. Math.,* 1985, vol. 80, no. 1, pp. 81–106.
32. Chenciner, A., Bifurcations de points fixes elliptiques: III. Orbites périodiques de "petites" périodes et élimination résonante des couples de courbes invariantes, *Inst. Hautes Études Sci. Publ. Math.,* 1987, vol. 66, pp. 5–91.
33. Chenciner, A. and Iooss, G., Bifurcations de tores invariants, *Arch. Ration. Mech. Anal.,* 1979, vol. 69, no. 2, pp. 109–198.
34. Chow, S.-N. and Hale, J. K., *Methods of Bifurcation Theory,* New York: Springer, 1982.
35. Ciocci, M. C., Litvak-Hinenzon, A., and Broer, H. W., Survey on Dissipative KAM Theory Including Quasi-Periodic Bifurcation Theory: Based on Lectures by Henk Broer, *Geometric Mechanics and Symmetry: The Peyresq Lectures*, J. Montaldi and T. Ratiu (Eds.), London Math. Soc. Lecture Note Ser., vol. 306, Cambridge: Cambridge Univ. Press, 2005, pp. 303–355.
36. Gómez, G., Mondelo, J.-M., and Simó, C., A Collocation Method for the Numerical Fourier Analysis of Quasi-Periodic Functions: I. Numerical Tests and Examples, *Discrete Contin. Dyn. Syst. Ser. B,* 2010, vol. 14, no. 1, pp. 41–74.
37. Gómez, G., Mondelo, J.-M., and Simó, C., A Collocation Method for the Numerical Fourier Analysis of Quasi-Periodic Functions: II. Analytical Error Estimates, *Discrete Contin. Dyn. Syst. Ser. B,* 2010, vol. 14, no. 1, pp. 75–109.
38. Guckenheimer, J. and Holmes, Ph., *Nonlinear Oscillations, Dynamical Systems, and Bifurcations of Vector Fields*, Appl. Math. Sci., vol. 42, New York: Springer, 1983.
39. Hanßmann, H., The Quasi-Periodic Centre-Saddle Bifurcation, *J. Differential Equations,* 1998, vol. 142, pp. 305–370.
40. Hanßmann, H., A Survey on Bifurcations of Invariant Tori, *New Advances in Celestial Mechanics and Hamiltonian systems (Guanajuato, 2001),* J. Delgado et al. (Eds.), New York: Kluwer/Plenum, 2004, pp. 109–121.
41. Hanßmann, H., *Local and Semi-Local Bifurcations in Hamiltonian Dynamical Systems: Results and Examples,* Lecture Notes in Math., vol. 1893, Berlin: Springer, 2007.
42. Haro, À. and de la Llave, R., A Parameterization Method for the Computation of Invariant Tori and Their Whiskers in Quasi-Periodic Maps: Rigorous Results, *J. Differential Equations,* 2006, vol. 228, no. 2, pp. 530–579.
43. Haro, À. and de la Llave, R., A Parameterization Method for the Computation of Invariant Tori and Their Whiskers in Quasi-Periodic Maps: Numerical Algorithms, *Discrete Contin. Dyn. Syst. Ser. B,* 2006, vol. 6, no. 6, pp. 1261–1300.
44. Haro, À. and de la Llave, R., A Parameterization Method for the Computation of Invariant Tori and Their Whiskers in Quasi-Periodic Maps: Explorations and Mechanisms for the Breakdown of Hyperbolicity, *SIAM J. Appl. Dyn. Syst.,* 2007, vol. 6, no. 1, pp. 142–207.
45. Hirsch, M. W., Pugh, C. C., and Shub, M., *Invariant Manifolds,* Lecture Notes in Math., vol. 583, Berlin–New York: Springer, 1977.
46. Iooss, G. and Los, J. E., Quasi-Genericity of Bifurcations to High-Dimensional Invariant Tori for Maps, *Comm. Math. Phys.,* 1988, vol. 119, no. 3, pp. 453–500.
47. Jorba, À., Numerical Computation of the Normal Behaviour of Invariant Curves of n-Dimensional Maps, *Nonlinearity,* 2001 vol. 14, no. 5, pp. 943–976.
48. Jorba, À. and Olmedo, E., On the Computation of Reducible Invariant Tori on a Parallel Computer, *SIAM J. Appl. Dyn. Syst.,* 2009, vol. 8, no. 4, pp. 1382–1404.
49. Jorba, À. and Tatjer, J. C., A Mechanism for the Fractalization of Invariant Curves in Quasi-Periodically Forced $1-D$ maps, *Discrete Contin. Dyn. Syst. Ser. B,* 2008, vol. 10, nos. 2–3, pp. 537–567.

50. de la Llave, R., González, A., Jorba, À., and Villanueva, J., KAM theory without Action-Angle Variables, *Nonlinearity,* 2005, vol. 18, no. 2, pp. 855–895.
51. Los, J., Dédoublement de courbes invariantes sur le cylindre: Petit diviseurs, *Ann. Inst. H. Poincaré Anal. Non Linéaire,* 1988, vol. 5, pp. 37–95.
52. Los, J., Non-Normally Hyperbolic Invariant Curves for Maps in $\mathbb{R}^3$ and Doubling Bifurcation, *Nonlinearity,* 1989, vol. 2, no. 1, pp. 149–174.
53. Lucarini, V., Speranza, A., and Vitolo, R., Parametric Smoothness and Self-Scaling of the Statistical Properties of a Minimal Climate Model: What beyond the Mean Field Theories?, *Phys. D,* 2007, vol. 234, no. 2, pp. 105–123.
54. Mondelo, J. M., Contribution to the Study of Fourier Methods for Quasi-Periodic Functions and the Vicinity of the Collinear Libration Points, *PhD thesis*, Univ. of Barcelona, 2001.
55. Newhouse, S. E., Palis, J., and Takens, F., Bifurcations and Stability of Families of Diffeomorphisms, *Inst. Hautes Études Sci. Publ. Math.,* 1983, vol. 57, pp. 5–71.
56. Puig, J. and Simó, C., Resonance Tongues and Spectral Gaps in Quasi-Periodic Schrödinger Operators with One or More Frequencies: A Numerical Exploration, *J. Dynam. Differential Equations,* 2011 (to appear).
57. Puig, J. and Simó, C., Resonance Tongues in the Quasi-Periodic Hill–Schrödinger Equation with Three Frequencies, *Regul. Chaotic Dyn.,* 2011, vol. 16, nos. 1–2, pp. 62–79.
58. Randriamampianina, A., Früh, W.-G., Maubert, P., and Read, P. L., Direct Numerical Simulations of Bifurcations in an Air-Filled Rotating Baroclinic Annulus *J. Fluid Mech.,* 2006, vol. 561, pp. 359–389.
59. Sánchez, J., Net, M., and Simó, C., Computation of Invariant Tori by Newton–Krylov Methods in Large-Scale Dissipative Systems, *Phys. D,* 2010, vol. 239, pp. 123–133.
60. Schilder, F., Osinga, H. M., and Vogt, W., Continuation of Quasi-Periodic Invariant Tori, *SIAM J. Appl. Dyn. Syst.,* 2005, vol. 4, no. 3, pp. 459–488.
61. Simó, C., Perturbations of Translations in the Two-Dimensional Torus: The Case near Resonance, *Proceedings VI CEDYA (Universidad de Zaragoza, Jaca, Spain, 1983),* Zaragoza, 1984.
62. Simó, C., On the Analytical and Numerical Computation of Invariant Manifolds, *Modern Methods in Celestial Mechanics,* D. Benest and C. Froeschlé (Eds.), Paris: Frontières, 1990, pp. 285–330. Available also at http://www.maia.ub.es/dsg/2004/.
63. Simó, C., Effective Computations in Hamiltonian Dynamics, *Mécanique celeste*, A. Chenciner and C. Simó (Eds.), SMF Journ. Annu., vol. 1996, Paris: Soc. Math. France, 1996.
64. C. Simó, Effective Computations in Celestial Mechanics and Astrodynamics. In *Modern Methods of Analytical Mechanics and their Applications (Udine, 1997)*, V. V. Rumyantsev and A. V. Karapetyan (Eds.), CISM Courses and Lectures, vol. 387, Vienna: Springer, 1998, pp. 55–102. Available also at http://www.maia.ub.es/dsg/1997/.
65. Takens, F. and Wagener, F. O. O., Resonances in Skew and Reducible Quasi-Periodic Hopf Bifurcations, *Nonlinearity,* 2000, vol. 13, no. 2, pp. 377–396.
66. van Veen, L., The Quasi-Periodic Doubling Cascade in the Transition to Weak Turbulence, *Phys. D*, 2005, vol. 210, nos. 3–4, pp. 249–261.
67. Vitolo, R., Bifurcations of Attractors in $3D$ Diffeomorphisms, *PhD thesis*, University of Groningen, 2003.
68. Vitolo, R., Broer, H. W., and Simó, C., Routes to Chaos in the Hopf-Saddle-Node Bifurcation for Fixed Points of $3D$-diffeomorphisms, *Nonlinearity,* 2010, vol. 23, no. 8, pp. 1919–1947.
69. Wagener, F. O. O., On the Quasi-Periodic d-fold Degenerate Bifurcation, *J. Differential Equations,* 2005, vol. 216, no. 2, pp. 261–281.
70. Wagener, F. O. O., A Parametrised Version of Moser's Modifying Terms Theorem, *Discrete Contin. Dyn. Syst. Ser. S,* 2010, vol. 3, no. 4, pp. 719–768.
71. Wagener, F. O. O., Semi-Local Analysis of the $k:1$ and $k:2$ Resonances in Quasi-Periodically Forced Systems, *Global Analysis of Dynamical Systems: Festschrift Dedicated to Floris Takens for His 60th Birthday,* H. W. Broer, B. Krauskopf, G. Vegter (Eds.), Bristol: Inst. Phys., 2001, pp. 113–129.
72. Wagener, F. O. O., On the skew Hopf bifurcation, *PhD Thesis,* University of Groningen, 1998.
73. Young, R. M. B. and Read, P. L., Flow Transitions Resembling Bifurcations of the Logistic Map in Simulations of the Baroclinic Rotating Annulus, *Phys. D,* 2008, vol. 237, no. 18, pp. 2251–2262.